Oscillatory periodic pattern dynamics in hyperbolic reaction-advection-diffusion models

Giancarlo Consolo [1,*] Carmela Curró,[1] Gabriele Grifó,[1] and Giovanna Valenti[2]

[1]*Department of Mathematical, Computer, Physical and Earth Sciences, University of Messina (Italy) V.le F. Stagno D'Alcontres 31, I-98166 Messina, Italy*

[2]*Department of Engineering, University of Messina (Italy) C.da di Dio, I-98166 Messina, Italy*

In this work we consider a quite general class of two-species hyperbolic reaction-advection-diffusion system with the main aim of elucidating the role played by inertial effects in the dynamics of oscillatory periodic patterns. To this aim, first, we use linear stability analysis techniques to deduce the conditions under which wave (or oscillatory Turing) instability takes place. Then, we apply multiple-scale weakly nonlinear analysis to determine the equation which rules the spatiotemporal evolution of pattern amplitude close to criticality. This investigation leads to a cubic complex Ginzburg-Landau (CCGL) equation which, owing to the functional dependence of the coefficients here involved on the inertial times, reveals some intriguing consequences. To show in detail the richness of such a scenario, we present, as an illustrative example, the pattern dynamics occurring in the hyperbolic generalization of the extended Klausmeier model. This is a simple two-species model used to describe the migration of vegetation stripes along the hillslope of semiarid environments. By means of a thorough comparison between analytical predictions and numerical simulations, we show that inertia, apart from enlarging the region of the parameter plane where wave instability occurs, may also modulate the key features of the coherent structures, solution of the CCGL equation. In particular, it is proven that inertial effects play a role, not only during transient regime from the spatially-homogeneous steady state toward the patterned state, but also in altering the amplitude, the wavelength, the angular frequency, and even the stability of the phase-winding solutions.

I. INTRODUCTION

Pattern formation and modulation is an active branch of mathematics, not only from the perspective of fundamental theory but also for its huge applications in many fields of physics, ecology, chemistry, biology, and other sciences [1–6]. In 1952, Turing proposed the mechanism through which a pattern-forming instability develops [7]. It arises from the coupling of diffusion and reaction kinetics, and is based on the destabilization of a spatially uniform steady state due to a perturbation of a given wave number.

The occurrence of such an instability is theoretically investigated by addressing, first, linear and, then, weakly nonlinear stability analysis. Linear stability analysis (LSA) is aimed at defining the critical threshold of the control parameter responsible for the instability. When addressing this study, it should be kept in mind that the simplest bifurcation of a spatially uniform steady state may result in the spontaneous formation of patterns that are oscillatory in time and uniform in space, stationary in time and periodic in space, or oscillatory in time and periodic in space. The primary bifurcations associated to these classes of patterns are classically identified as Hopf,

Turing, and wave (also named Turing-Hopf or oscillatory-Turing), respectively [8].

Weakly nonlinear stability analysis (WNA) is focused on deducing the equation governing the evolution of pattern amplitude (or envelope) close to criticality. In spatially extended systems, pattern amplitude is usually ruled by the well-known (real or complex) Ginzburg-Landau equation, which represents a general normal-form type of equation, valid for a large class of bifurcations and nonlinear wave phenomena occurring in many areas of sciences [1,2,5,6,9–18]. In particular, when applied to the study of oscillatory periodic patterns, the Ginzburg-Landau equation has complex coefficients and does not have a Lyapunov functional [1,2,5,6,19–23]. Its simplest solutions are in the form of coherent structures, among which plane-wave (or traveling-wave) solutions represent the easiest and most intuitive example.

In this work we focus our attention on the occurrence of wave instability with the goal of characterizing the dynamics of traveling patterns in one-dimensional *hyperbolic* reaction-advection-diffusion systems for two interacting species. In particular, by using the above-mentioned tools of LSA and WNA, we aim at elucidating the role played by inertia in modifying the instability threshold, the key features of the emerging patterns, and their stability.

This work is an attempt to provide a step forward towards a deeper understanding of the underlying mechanisms involved into the formation of traveling patterns in hyperbolic models. Indeed, the goal is to extend the literature of hyperbolic systems that encloses several related works focusing, for instance, on wave instability in systems where one species

---

*Corresponding author: gconsolo@unime.it

diffuses and the other ones undergoes advection, by adopting LSA only [24]; Turing and wave instabilities in the presence of cross-diffusion, with no advection, by adopting LSA and WNA in limited domains [25] or LSA only [8,26]; Turing instability in the absence of advection, by using LSA and WNA in extended domains with constant [27–29] and nonconstant [30] inertial times; traveling fronts in models with advection [31,32] or in its absence considering self-diffusion [33] and cross-diffusion [34].

As widely outlined in all the above-mentioned works, the use of an hyperbolic framework has a manifold justification. First, it is well known that parabolic models suffer from the paradox of infinite propagation speed of disturbances, whereas hyperbolic models overcome this problem by accounting for relaxational effects due to the delay of the species in adopting one definite mean speed and direction to propagate [32]. Therefore, these latter are better suited to describe transient regimes, especially those involving long timescales. Moreover, the inertial (delay) times constitute additional degrees of freedom that may be used to better mimic experimental observations and, at the same time, offer a richer scenario of dynamics [28,29,35–45].

The theoretical predictions here carried out are then corroborated by numerical investigations on the so-called extended Klausmeier model, taken into account as an illustrative example of a two-species system where the combination of kinetics, diffusion, and advection gives rise to oscillatory periodic patterns. It is a conceptual model for surface water and vegetation biomass, used to describe the formation and migration of vegetation patterns over sloping terrains of semiarid ecosystems. This model, among many others [46–50], aims at exploring the processes of desertification occurring in such drylands areas [51–55]. In its original formulation [56], this model accounted for the isotropic diffusion of vegetation and the anisotropic advection of water along the hillslope. Later [57], this model has been extended to account also for diffusion of water and, in [58], it has been further generalized to include the phenomenon of secondary-seed dispersal. All the above models are able to capture the uphill migration of vegetation bands, which are believed to be observed experimentally [45,59]. Moreover, to account for the relevance of biological inertia in plant communities to ecology of arid ecosystems [36,42,44] as well as to provide a proper description of long transient pattern dynamics [60–63], hyperbolic generalizations of Klausmeier model have been proposed in [24,27,30,31].

The paper is outlined as follows. In Sec. II, we present the class of hyperbolic reaction-advection-diffusion models and characterize the phenomenon of wave instability through LSA and WNA. In Sec. III, we compare our results of analytical predictions to those arising from numerical simulations, carried out on the hyperbolic version of the extended Klausmeier model. Conclusions are given in the last section.

II. MODEL FORMULATION AND ANALYTICAL INVESTIGATIONS

We consider a class of hyperbolic reaction-advection-diffusion systems for two species $u(x, t)$ and $w(x, t)$ satisfying the following hypotheses: dynamics takes place at time t and

along a preferred direction x; w undergoes both diffusion and advection with a velocity denoted by v, whereas u has a diffusive character only; the w-by-u diffusion ratio is termed d; the inertial times associated to the two species are denoted by τ^u and τ^w, which are assumed to be constant; kinetic terms are generically indicated by $f(u, w)$ and $g(u, w)$. Following the guidelines of extended thermodynamics (ET) theory [64], we also introduce two additional field variables representing the diffusive fluxes $J^u(x, t)$ and $J^w(x, t)$, each of them obeying a thermodynamically consistent balance equation that, in the parabolic limit approximation, $\tau^u \to 0$ and $\tau^w \to 0$, recover the classical constitutive Fick's law.

According to these assumptions, the hyperbolic system can be expressed in vector form as

$$\mathbf{U}_t + M\mathbf{U}_x = \mathbf{N}(\mathbf{U}), \qquad (1)$$

being

$$\mathbf{U} = \begin{bmatrix} u \\ w \\ J^u \\ J^w \end{bmatrix}, \quad M = \begin{bmatrix} 0 & 0 & 1 & 0 \\ 0 & -v & 0 & 1 \\ \frac{1}{\tau^u} & 0 & 0 & 0 \\ 0 & \frac{d}{\tau^w} & 0 & 0 \end{bmatrix}, \quad \mathbf{N}(\mathbf{U}) = \begin{bmatrix} f(u, w) \\ g(u, w) \\ -\frac{J^u}{\tau^u} \\ -\frac{J^w}{\tau^w} \end{bmatrix}, \qquad (2)$$

where the subscript stands for the partial derivative with respect to the indicated variable. Note that the model (2) belongs to a more general class of n-species hyperbolic reaction-advection-diffusion systems deduced via ET and reported in [31].

In the following sections, we will address LSA and WNA on the steady states admitted by this model with particular emphasis on the occurrence of wave instability.

A. Linear stability analysis

Let $\mathbf{U}^* = (u^*, v^*, 0, 0)$ be a positive spatially homogeneous steady state satisfying $\mathbf{N}(\mathbf{U}) = \mathbf{0}$. By looking for solutions of system (1) of the form $\mathbf{U} = \mathbf{U}^* + \widehat{\mathbf{U}} \exp(\omega t + ik x)$, we derive the following dispersion relation which gives the growth factor ω as a function of the wave number k:

$$\tau^u \tau^w \omega^4 + (\widetilde{A}_3 - ikv\tau^u\tau^w)\omega^3 + (\widehat{A}_2 k^2 + \widetilde{A}_2 + ikv\widehat{b}_2)\omega^2$$
$$+ [\widehat{A}_1 k^2 + \widetilde{A}_1 + ikv(\widehat{b}_1 - \tau^w k^2)]\omega + \widetilde{A}_0 + ikv\widehat{b}_0 = 0 \qquad (3)$$

with

$$\widetilde{A}_3 = \tau^u + \tau^w - (f_u^* + g_w^*)\tau^u\tau^w,$$
$$\widehat{A}_2 = d\tau^u + \tau^w,$$
$$\widetilde{A}_2 = 1 - (\tau^u + \tau^w)(f_u^* + g_w^*) + \tau^u\tau^w(f_u^* g_w^* - f_w^* g_u^*),$$
$$\widehat{b}_2 = \tau^u\tau^w f_u^* - \tau^u - \tau^w,$$
$$\widehat{A}_1 = d + 1 - \tau^w g_w^* - d\tau^u f_u^*,$$
$$\widetilde{A}_1 = (\tau^u + \tau^w)(f_u^* g_w^* - f_w^* g_u^*) - (f_u^* + g_w^*),$$
$$\widehat{b}_1 = (\tau^u + \tau^w)f_u^* - 1,$$
$$\widetilde{A}_0 = dk^4 - (df_u^* + g_w^*)k^2 + f_u^* g_w^* - f_w^* g_u^*,$$
$$\widehat{b}_0 = f_u^* - k^2, \qquad (4)$$

where the asterisk denotes that the function is evaluated at the steady state $\mathbf{U}^*$.

It is straightforward to ascertain that, for homogeneous perturbation $k = 0$, Eq. (3) can be easily factorized and its solutions are

$$\omega_1 = -\frac{1}{\tau^u} < 0, \quad \omega_2 = -\frac{1}{\tau^w} < 0,$$

$$\omega_{3,4} = \frac{1}{2}\left[f_u^* + g_w^* \pm \sqrt{(f_u^* + g_w^*)^2 - 4(f_u^* g_w^* - f_w^* g_u^*)} \right].$$

(5)

Therefore, $\mathbf{U}^*$ is stable with respect to homogeneous perturbation iff

$$f_u^* + g_w^* < 0, \quad f_u^* g_w^* - f_w^* g_u^* > 0.$$

(6)

As far as nonhomogeneous perturbations are concerned, we notice that a nonvanishing advection term ($\nu \neq 0$) prevents the occurrence of Turing instability, because the expression $\widehat{A}_0 + ik\nu\widehat{b}_0$ is nonzero for all values of k. Therefore, we focus our attention on the occurrence of wave instability as a control parameter, say B, is varied. To this aim, we look for solutions of the characteristic equation (3) having null real part for some $k \neq 0$ and require the transition from negative to positive real part to occur via a maximum. More precisely, we assume $\omega = -isk$, with $s = s(k) \in \mathbb{R}$ so that any perturbation can be recast in the form of a traveling plane wave with speed s, i.e., $\widehat{\mathbf{U}} \exp[ik(x - st)]$. Then, by substituting the previous ansatz into the characteristic equation and taking the derivative of this latter with respect to k, we obtain

$$k^4 - \delta_2 k^2 + \delta_4 = 0,$$

$$\delta_1 k^2 - \delta_3 = 0,$$

$$2k(2k^2 - \delta_2) + \left(\frac{\partial \delta_4}{\partial s} - \frac{\partial \delta_2}{\partial s} k^2 \right) \frac{\partial s}{\partial k} = 0,$$

$$(\delta_1 \delta_2 - 2\delta_3)\left(\delta_1 \frac{\partial \delta_3}{\partial s} - \delta_3 \frac{\partial \delta_1}{\partial s} \right) - \delta_1^2 \left(\delta_1 \frac{\partial \delta_4}{\partial s} - \delta_3 \frac{\partial \delta_2}{\partial s} \right) = 0,$$

(7)

where

$$\delta_1 = \frac{\nu + \widehat{A}_1 s + \nu\widehat{b}_2 s^2 - \widetilde{A}_3 s^3}{(\tau^u s^2 - 1)(\tau^w s^2 + \nu\tau^w s - d)},$$

$$\delta_2 = \frac{\widetilde{A}_2 s^2 - \widehat{b}_1 \nu s + d f_u^* + g_w^*}{(\tau^u s^2 - 1)(\tau^w s^2 + \nu\tau^w s - d)},$$

$$\delta_3 = \frac{\nu f_u^* - \widetilde{A}_1 s}{(\tau^u s^2 - 1)(\tau^w s^2 + \nu\tau^w s - d)},$$

$$\delta_4 = \frac{(f_u^* g_w^* - f_w^* g_u^*)}{(\tau^u s^2 - 1)(\tau^w s^2 + \nu\tau^w s - d)}.$$

(8)

System (7) defines implicitly the critical value B_c of the control parameter at which wave instability develops, together with the critical wave number k_c, the wave speed s, and its derivative with respect to the wave number $\partial s/\partial k$. Therefore, we can draw a first conclusion that the presence of inertia affects not only the instability threshold, but also the wave number of the emerging pattern. This result differs from what observed in the case of pure stationary Turing patterns, where hyperbolicity does not affect such quantities but plays an active role during transient regime [27,30].

Notice that in the limit case $\tau^u \to 0$ and $\tau^w \to 0$ the hyperbolic model (1), (2) reduces to the corresponding *parabolic* one. Details on the structure of the parabolic model, the characteristic equation, and the locus of wave instability are given in Appendix A.

B. Multiple-scale weakly nonlinear analysis

As it is well known, LSA is only valid for small times and infinitesimal perturbations. For this reason, the transition to the new spatially nonuniform state is usually investigated by means of WNA which, by using a standard perturbative approach, provides an approximate analytical description of the perturbation dynamics. In this section, we shall employ the multiple-scale method to derive the amplitude equation describing the dynamics close to the critical bifurcation parameter B_c at which instability develops [5,6,25,27–29, 65–67].

We recast the original system (1) in the following form:

$$\overline{\mathbf{U}}_t + M\overline{\mathbf{U}}_x = L^*\overline{\mathbf{U}} + \mathbf{NL}^*,$$

(9)

where the matrix L^* and the vectors $\overline{\mathbf{U}}$ and $\mathbf{NL}^*$ are defined as

$$\overline{\mathbf{U}} = \mathbf{U} - \mathbf{U}^*,$$

(10)

$$L^* = (\nabla \mathbf{N})^*,$$

(11)

$$\mathbf{NL}^* = \sum_{k \geqslant 2} \frac{1}{k!}[(\overline{\mathbf{U}} \cdot \nabla)^{(k)}\mathbf{N}]^*,$$

(12)

and $\nabla = \partial/\partial\mathbf{U}$, for a generic vector $\mathbf{V}$, the expression $(\mathbf{V} \cdot \nabla)^{(j)}$ stands for the operator

$$\mathbf{V} \cdot \nabla = V_1 \frac{\partial}{\partial u} + V_2 \frac{\partial}{\partial w} + V_3 \frac{\partial}{\partial J^u} + V_4 \frac{\partial}{\partial J^w}$$

(13)

applied j times.

First, we expand the field vector $\overline{\mathbf{U}}$ as well as the control parameter B with respect to a small positive parameter $\varepsilon \ll 1$ and introduce two time and spatial scales as follows:

$$\overline{\mathbf{U}} = \varepsilon\overline{\mathbf{U}}_1 + \varepsilon^2\overline{\mathbf{U}}_2 + \varepsilon^3\overline{\mathbf{U}}_3 + O(\varepsilon^4),$$

$$B = B_c + \varepsilon^2 B_2 + O(\varepsilon^4),$$

$$\frac{\partial}{\partial t} \to \frac{\partial}{\partial t} + \varepsilon^2 \frac{\partial}{\partial T_2},$$

$$\frac{\partial}{\partial x} \to \frac{\partial}{\partial x} + \varepsilon \frac{\partial}{\partial X}.$$

(14)

The use of two spatial scales is justified whenever patterns emerge and propagate over large spatial domains in the form of traveling wavefronts.

Then, substituting all the above expansions into the governing system (9) and collecting terms of the same orders of ε we obtain the following set of linear partial differential equations:

at order 1 $$\frac{\partial \overline{\mathbf{U}}_1}{\partial t} + M\frac{\partial \overline{\mathbf{U}}_1}{\partial x} = L_c^* \overline{\mathbf{U}}_1,$$

at order 2 $$\frac{\partial \overline{\mathbf{U}}_2}{\partial t} + M\frac{\partial \overline{\mathbf{U}}_2}{\partial x} + M\frac{\partial \overline{\mathbf{U}}_1}{\partial X} = L_c^* \overline{\mathbf{U}}_2 + \frac{1}{2}\left(\overline{\mathbf{U}}_1 \cdot \nabla\right)^{(2)}\mathbf{N}|_c^*,$$

at order 3 $$\frac{\partial \overline{\mathbf{U}}_3}{\partial t} + \frac{\partial \overline{\mathbf{U}}_1}{\partial T_2} + M\frac{\partial \overline{\mathbf{U}}_3}{\partial x} + M\frac{\partial \overline{\mathbf{U}}_2}{\partial X} = L_c^* \overline{\mathbf{U}}_3 + B_2\frac{dL^*}{dB}\bigg|_c \overline{\mathbf{U}}_1 + (\overline{\mathbf{U}}_1 \cdot \nabla)(\overline{\mathbf{U}}_2 \cdot \nabla)\mathbf{N}|_c^* + \frac{1}{6}\left(\overline{\mathbf{U}}_1 \cdot \nabla\right)^{(3)}\mathbf{N}|_c^*, \qquad (15)$$

where the subscript "c" denotes that the quantity is evaluated at the critical value of the control parameter. We now look for solution $\overline{\mathbf{U}}_i = \overline{\mathbf{U}}_i(z)$ with $z = x - st$, so that the system (15) can be written as a system of ordinary differential equations:

at order 1 $$\frac{d\overline{\mathbf{U}}_1}{dz} = K_c^* \overline{\mathbf{U}}_1, \qquad (16)$$

at order 2 $$\frac{d\overline{\mathbf{U}}_2}{dz} = K_c^* \overline{\mathbf{U}}_2 + (M - sI)^{-1}\left\{\frac{1}{2}\left(\overline{\mathbf{U}}_1 \cdot \nabla\right)^{(2)}\mathbf{N}|_c^* - M\frac{\partial \overline{\mathbf{U}}_1}{\partial X}\right\}, \qquad (17)$$

at order 3 $$\frac{d\overline{\mathbf{U}}_3}{dz} = K_c^* \overline{\mathbf{U}}_3 + (M - sI)^{-1}\left\{B_2\frac{dL^*}{dB}\bigg|_c \overline{\mathbf{U}}_1 + \left(\overline{\mathbf{U}}_1 \cdot \nabla\right)\left(\overline{\mathbf{U}}_2 \cdot \nabla\right)\mathbf{N}|_c^* + \frac{1}{6}\left(\overline{\mathbf{U}}_1 \cdot \nabla\right)^{(3)}\mathbf{N}|_c^* - \frac{\partial \overline{\mathbf{U}}_1}{\partial T_2} - M\frac{\partial \overline{\mathbf{U}}_2}{\partial X}\right\}, \quad (18)$$

where I is the identity matrix and

$$K_c^* = (M - sI)^{-1}L_c^*. \qquad (19)$$

According to WNA developed in Appendix B, the solutions of systems (16) and (17), satisfying periodic boundary conditions, take, respectively, the following structures:

$$\overline{\mathbf{U}}_1 = \Omega(X, T_2)e^{ik_c z}\mathbf{d}^{(ik_c)} + \overline{\Omega}(X, T_2)e^{-ik_c z}\mathbf{d}^{(-ik_c)}, \qquad (20)$$

$$\overline{\mathbf{U}}_2 = \frac{\partial \Omega}{\partial X}e^{ik_c z}\mathbf{g} + \frac{\partial \overline{\Omega}}{\partial X}e^{-ik_c z}\overline{\mathbf{g}} + \Omega^2 e^{2ik_c z}\mathbf{q} + \overline{\Omega}^2 e^{-2ik_c z}\overline{\mathbf{q}} + 2\mathbf{q}_0|\Omega|^2, \qquad (21)$$

where the complex pattern amplitude Ω obeys the cubic complex Ginzburg-Landau (CCGL) equation

$$\frac{\partial \Omega}{\partial T_2} = (\rho_1 + i\rho_2)\frac{\partial^2 \Omega}{\partial X^2} + (\sigma_1 + i\,\sigma_2)\Omega - (L_1 - iL_2)\Omega\,|\Omega|^2. \qquad (22)$$

The coefficients appearing in (20)–(22) are given in Appendix B.

As known, two different qualitative dynamics of the CCGL equation can be observed: $L_1 > 0$ corresponds to the supercritical bifurcation case while $L_1 < 0$ to the subcritical one. The former exists for above-threshold values of the control parameter only, exhibits a small amplitude close to onset, and the wavelength of the excited pattern is close to the critical value $2\pi/k_c$. The latter exists for both below- and above-threshold values, exhibits hysteresis, and has a large amplitude at onset such that the WNA may only provide qualitative information on the excited patterns [1,5,6].

Remark 1. The CCGL equation (22) deduced in the more general framework of hyperbolic systems appears formally unchanged with respect to the classical one deduced in *parabolic* models [67]. It can be indeed verified that the expressions of the coefficients there appearing may be obtained from the ones appearing in (22) by setting the inertial times to zero. Of course, each of these coefficients encloses a dependence on the inertial times which, acting as additional degrees of freedom, offers a richer scenario of spatiotemporal dynamics with respect to the parabolic counterpart, as it will be shown below.

Coherent structure solutions of the CCGL equation

Let us now focus our attention on those solutions of the CCGL equation that are referred to as *coherent structures*, and in particular to the one-parameter family of solutions localized in space characterized by features uniformly translating with a constant velocity v [1,5,19–23], i.e.,

$$\Omega(X, T_2) = Q(\xi)e^{i\phi(\xi)}, \qquad \xi = X - vT_2. \qquad (23)$$

Substituting this ansatz into the CCGL equation (22) and indicating by $\kappa = \phi_\xi$, we get a system of three ordinary differential equations:

$$Q_\xi = R,$$

$$\rho_2 Q\kappa_\xi - \rho_1 R_\xi = (v - 2\rho_2\kappa)R + (\sigma_1 - \rho_1\kappa^2)Q - L_1 Q^3,$$

$$\rho_2 R_\xi + \rho_1 Q\kappa_\xi = -2\rho_1\kappa R + (\rho_2\kappa^2 - \sigma_2 - v\kappa)Q - L_2 Q^3.$$

$$(24)$$

The dynamical system (24) admits two fixed points in the form $\mathbf{F}^* = (R^*, Q^*, \kappa^*)$ given by $\mathbf{F}_1^* = (0, 0, \kappa_0)$, with κ_0 an arbitrary constant, and $\mathbf{F}_2^* = (0, \widetilde{Q}, \widetilde{\kappa})$, where the constants $\widetilde{Q}$ and $\widetilde{\kappa}$ are defined by

$$\widetilde{Q} = \sqrt{\frac{\sigma_1 - \rho_1 \widetilde{\kappa}^2}{L_1}},$$

$$(\rho_1 L_2 + \rho_2 L_1)\widetilde{\kappa}^2 - v L_1 \widetilde{\kappa} - (\sigma_2 L_1 + \sigma_1 L_2) = 0. \quad (25)$$

The fixed point $\mathbf{F}_1^*$ defines a null-amplitude patterned state $\Omega = 0$ that is representative of the spatially homogeneous steady state $\mathbf{U}^*$ undergoing the spatially driven destabilization. On the other hand, the plane-wave solution of the CCGL equation associated to the fixed point $\mathbf{F}_2^*$, i.e.,

$$\Omega(X, T_2) = \widetilde{Q} e^{i(\widetilde{\kappa} X + \widetilde{\omega} T_2)} \quad \text{with} \quad \widetilde{\omega} = -\widetilde{\kappa} v \quad (26)$$

represents a particular case of coherent structure named *phase-winding* solution [1,5,21,23,68] and describes a traveling pattern characterized by a total wave number $k_{\text{tot}} = k_c + \epsilon \widetilde{\kappa}$ and angular frequency $\omega_{\text{tot}} = k_c s - \epsilon^2 \widetilde{\omega}$. If the wave bifurcation is supercritical ($L_1 > 0$), under the assumptions that $\sigma_1 > 0$ and $\rho_1 > 0$, according to the first eq. in (25), such a solution exists if

$$-\sqrt{\frac{\sigma_1}{\rho_1}} < \widetilde{\kappa} < +\sqrt{\frac{\sigma_1}{\rho_1}} \quad (27)$$

so that there is a band of permitted wave numbers around $\widetilde{\kappa} = 0$ and the second-order correction of the angular frequency takes the form

$$\widetilde{\omega} = [(\sigma_2 L_1 + \sigma_1 L_2) - (\rho_1 L_2 + \rho_2 L_1)\widetilde{\kappa}^2]/L_1. \quad (28)$$

Since we deal with three unknowns ($\widetilde{\kappa}$, $\widetilde{Q}$, and $\widetilde{\omega}$) and two conditions arising from the CCGL equation, one parameter needs to be estimated from numerical simulations. For instance, $\widetilde{\kappa}$ can be deduced by comparing the numerically computed value of the total wave number k_{tot} with the theoretical critical wave number k_c, whereas the values of amplitude $\widetilde{Q}$ and angular frequency $\widetilde{\omega}$ can be consequently obtained via (25) and (28), respectively.

To investigate the stability of the phase-winding solution, we can proceed, as usual in the literature, by perturbing the amplitude (26) as follows:

$$\Omega(X, T_2) = [1 + a(X, T_2)]\widetilde{Q} e^{i(\widetilde{\kappa} X + \widetilde{\omega} T_2)},$$

$$a(X, T_2) = \Psi(T_2)e^{ilX} + \overline{\Xi}(T_2)e^{-ilX} \quad (29)$$

with l the small perturbation of the wave number $\widetilde{\kappa}$, namely, we look for long-wave effects. After some algebraic manipulations, we end up with the system

$$\Psi_{T_2} = [-l(l + 2\widetilde{\kappa})(\rho_1 + i\rho_2) - \widetilde{Q}^2(L_1 - iL_2)]\Psi$$
$$- (L_1 - iL_2)\widetilde{Q}^2 \Xi,$$

$$\Xi_{T_2} = [-l(l - 2\widetilde{\kappa})(\rho_1 - i\rho_2) - \widetilde{Q}^2(L_1 + iL_2)]\Xi$$
$$- (L_1 + iL_2)\widetilde{Q}^2 \Psi, \quad (30)$$

where $\overline{\Xi}$ is the complex conjugate of Ξ.

Then, looking for the usual exponential dependence of Ψ and Ξ on T_2, in the limit of large wavelengths (small l), one retrieves a necessary condition for the stability of

plane-wave structures, named *Benjamin-Feir-Newell* condition [1,2,6,23,67], that reads as

$$1 - \frac{\rho_2 L_2}{\rho_1 L_1} > 0. \quad (31)$$

Remark 2. It should be finally noticed that all the features characterizing the phase-winding solution, i.e., amplitude $\widetilde{Q}$, wave number $\widetilde{\kappa}$, and angular frequency $\widetilde{\omega}$, together with its stability, inherit the functional dependence on the inertial times from the coefficients of the CCGL equation (22). Therefore, it is expected that hyperbolicity effects may manifest, not only during the transient regime from the homogeneous steady state toward the patterned state [the heteroclinic orbit of (24) joining $\mathbf{F}_1^*$ and $\mathbf{F}_2^*$], but also modifying the value of the above-mentioned key features of the phase-winding solution and, possibly, its stability.

III. AN ILLUSTRATIVE EXAMPLE: THE EXTENDED KLAUSMEIER MODEL

As an illustrative example, let us take into account the hyperbolic generalization [24,27,30,31] of the extended Klausmeier model [57,67], whose dimensionless one-dimensional (1D) version belongs to the class of systems (1), (2). In this framework, the field variables $u(x, t)$ and $w(x, t)$ assume the meaning of densities of plant biomass and surface water, respectively, at location x (positive direction being uphill) and time t. In this model, the motion of surface water accounts for two different mechanisms. First, the downhill water flow on slopes is accounted by an advection term. Second, dispersal of surface water is mimicked via a diffusion term that aims at capturing the movement induced by spatial differences in infiltration rate [57]. The coefficient d is here representative of the water-to-plant diffusion ratio whereas v is the water advection speed along the hill slope. The source terms, unchanged with respect to those originally proposed by Klausmeier [56], are given by

$$f(u, w) = w u^2 - B u,$$
$$g(u, w) = A - w - w u^2, \quad (32)$$

where the dimensionless coefficients A and B are related to the rates of average annual rainfall and plant loss, respectively. Previous investigations suggest that realistic values of plant loss and rainfall rate belong to the ranges $B \in (0, 2)$ and $A \in (0, 3)$, respectively [47,56,69].

It is known that for $A \geqslant 2B$ this model admits three spatially homogeneous steady states given by

$$\mathbf{U}_D^* = (0, A, 0, 0),$$
$$\mathbf{U}_L^* = (u_L, B/u_L, 0, 0)$$
$$\mathbf{U}_S^* = (u_S, B/u_S, 0, 0), \quad (33)$$

where

$$u_L = \frac{A - \sqrt{A^2 - 4B^2}}{2B},$$

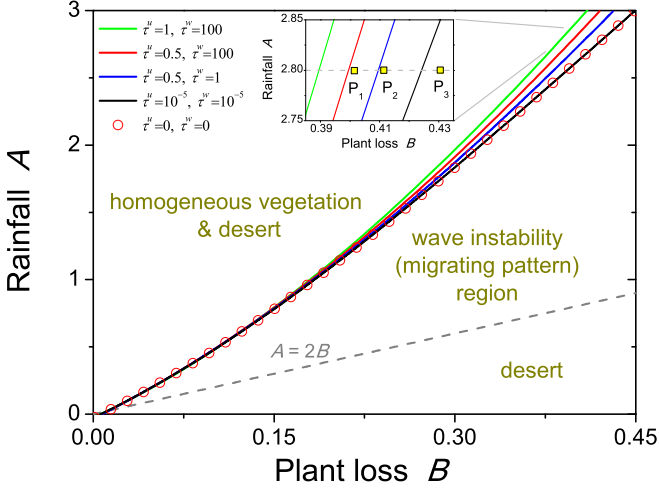$$u_S = \frac{A + \sqrt{A^2 - 4B^2}}{2B}, \quad 0 < u_L < 1 < u_S \quad (34)$$

FIG. 1. Solid lines represent the loci of wave instability in the (B, A) parameter plane obtained by solving numerically the system (7), (8) for different values of inertial times. Symbols denote the locus obtained in the parabolic case, resulting from integration of Eq. (A4). The bottom dashed line defines the condition $A = 2B$, below which the only desert state exists. Fixed parameters: $d = 100$ and $\nu = 182.5$.

the first being representative of the desert state and the other ones of uniformly vegetated areas. For $A < 2B$, the desert state becomes the only steady state admitted by the model.

It can be easily checked that the desert state $\mathbf{U}_D^*$ is always stable whereas the vegetated state $\mathbf{U}_L^*$ is always unstable. On the contrary, the state $\mathbf{U}_S^*$ is stable with respect to homogeneous perturbations. Indeed, by considering that

$$
\begin{aligned}
f_u^* = f_u(\mathbf{U}_S^*) = B, \quad & f_w^* = f_w(\mathbf{U}_S^*) = u_S^2, \\
g_u^* = g_u(\mathbf{U}_S^*) = -2B, \quad & g_w^* = g_w(\mathbf{U}_S^*) = -(1 + u_S^2),
\end{aligned}
\tag{35}
$$

conditions (6) become

$$
\begin{aligned}
f_u^* + g_w^* = B - 1 - u_S^2 < 0, \\
f_u^* g_w^* - f_w^* g_u^* = B(u_S^2 - 1) > 0,
\end{aligned}
\tag{36}
$$

that are fulfilled for any realistic values of B and u_S.

To prove that the state $\mathbf{U}_S^*$ may be destabilized via non-homogeneous perturbations, and can thus undergo wave instability, we need to solve the system (7), (8). Unfortunately, owing to its highly nonlinear nature, information on the locus of wave instability, together with the dependence of the critical parameters on the inertial times, cannot be obtained analytically. Therefore, by solving the above system numerically, we found that it admits real solutions representing the values of the control parameter B_c, wave number k_c, wave speed s, and its derivative with respect to k, at the onset of instability. Results of this investigation are shown in Fig. 1, where the locus of wave instability depicted in the (B, A) parameter plane (solid lines) is obtained by fixing the parameters $d = 100$ [57,70] and $\nu = 182.5$ [56] and varying the two inertial times τ^u and τ^w. In the same figure we also represent by circles the locus obtained in the parabolic case, i.e., from the numerical solution of (A4), which gives real and positive roots by taking the plus sign. As it can be noticed, this latter

coincides with the locus deduced for very small inertial times (black line), as expected. It is worth noticing that, when the system moves away from the parabolic limit, the locus of wave instability progressively shifts up so enlarging the region where nonstationary patterns may be observed. This is consistent with our previous results obtained for the hyperbolic generalization of the original Klausmeier model, so confirming that the hyperbolicity destabilizes the system and allows to observe oscillatory periodic patterns, i.e., uphill migrating banded vegetation in the context of dry-land ecology, over a wider region of the parameter plane [24].

A first check on the validity of these analytical predictions has been carried out by inspecting the wave-number dependence of the four roots of the characteristic polynomial (3) at the three points P_1, P_2, and P_3 indicated in the inset of Fig. 1, for different couples of inertial times. Results are shown in Fig. 2 [top row panels (a)–(c) correspond to P_1, middle row panels (d)–(f) to P_2, and bottom row panels (g)–(i) to P_3] for the largest eigenvalue only (being the real part of the other three roots always negative). For brevity, we refer to the couple $(\tau^u, \tau^w) = (10^{-5}, 10^{-5})$ (whose corresponding locus is the black curve in Fig. 1) as setup *I*; the couple $(0.5, 1)$ as setup *II* (blue curve in Fig. 1), and $(0.5, 100)$ as setup *III* (red curve in Fig. 1). Setup *I* is representative of the behavior close to the parabolic limit, while setups *II* and *III* mimic dynamics that progressively deviate away from it.

Let us investigate, first, the locus of roots related to P_1. Results related to setups *I* and *II* [Figs. 2(a) and 2(b)] reveal that all roots have negative real part, denoting that the state $\mathbf{U}_S^*$ is also stable with respect to nonhomogeneous perturbations. On the contrary, in setup *III* [Fig. 2(c)], there exists a range of wave number where one root has positive real part and non-null imaginary part, so pointing out a destabilization of the steady state. These observations are consistent with the predictions reported in Fig. 1 because, in setups *I* and *II*, the investigated point is outside the wave instability region but, in setup *III*, it is located inside. About the point P_2, in setups *II* and *III* [Figs. 2(e) and 2(f)] there exists a range of k where the real part of the most unstable root becomes positive. On the contrary, in setup *I* [Fig. 2(d)], the real part of this root keeps negative, consistently with its location with respect to the bifurcation loci. Finally, at point P_3, for each of the chosen setups [Figs. 2(g)–2(i)], there exists a range of k where the real part of the most unstable root becomes positive, consistently with the fact that this point always lies inside the wave instability region.

Another confirmation of the analytical predictions carried out in Sec. II A may be achieved by integrating numerically the governing system (1), (2), (32) together with periodic boundary conditions and using small sinusoidal fluctuations about the steady state $\mathbf{U}_S^*$ as initial conditions. Simulations have been performed by means of COMSOL MULTIPHYSICS® [71] over a time window $t \in [0, 50]$, considering a spatial domain of length $l_D = 100$ (unless specified differently). Results of this investigation, which make use of the same parameter set as the one used in Fig. 2, are reported in Fig. 3. To provide an immediate and intuitive view of the underlying dynamics, the color map used for the density plots of vegetation biomass $u(x, t)$ ranges between yellow (desert) and green (vegetated areas). In agreement with the above-mentioned predictions,
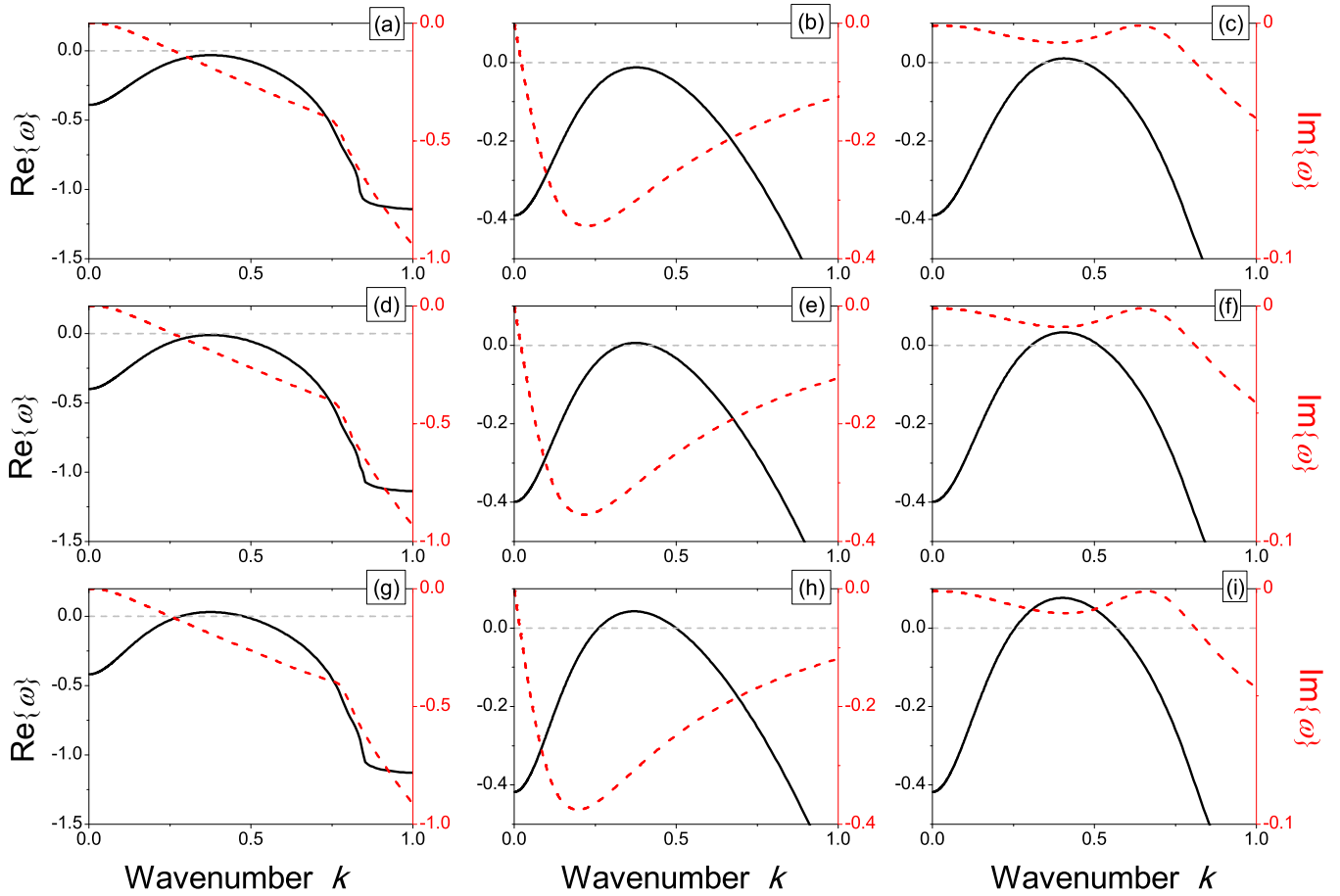
FIG. 2. Wave-number dependence of the real (left axes, continuous lines) and imaginary (right axes, discontinuous lines) parts of largest root of (3) evaluated for $A = 2.8$ at the points P$_1$ [$B = 0.40$, (a)–(c)], P$_2$ [$B = 0.41$, (d)–(f)], and P$_3$ [$B = 0.43$, (g)–(i)] indicated in Fig. 1, for different couples of inertial times (τ^u, τ^w). In detail, setup *I*: $(10^{-5}, 10^{-5})$, (a), (d), (g); setup *II*: (0.5,1), (b), (e), (h); setup *III*: (0.5,100), (c), (f), (i).

it is possible to notice that, when all the roots have negative real parts, the initial perturbation dies out and the system converges toward the stable, spatially uniform, vegetated state $\mathbf{U}_S^*$ [see Figs. 3(a), 3(b), and 3(d)]. On the contrary, if there exists a range of unstable wave numbers, then the system evolves toward a periodic patterned state that oscillates in time, representative of an uphill migrating vegetation band [see Figs. 3(c) and 3(e)–3(i)].

We can also numerically verify whether the range of unstable wave numbers depends on inertia. It is known that, if a nonhomogeneous perturbation is applied to a state $\mathbf{U}^*$ falling within the wave instability region, the system tends to form a traveling pattern whose wave number is close to the one of the most unstable mode, i.e., the mode exhibiting the largest growth rate. The range of unstable wave numbers that is created when the control parameter is above the critical value B_c degenerates into the single value k_c at onset. To address this point, we track the variations in the (B, k) plane of the root of the characteristic polynomial (3) associated to the most unstable mode, for different values of inertial times. Results are shown in Fig. 4, where the wave number of the mode exhibiting the largest growth rate is depicted by dashed lines whereas the range of unstable wave numbers is delimited by solid lines. When we move away from the parabolic limit

(from black to red curves in the figure), the role played by inertia becomes manifold: it decreases the lowest value of the control parameter (plant loss) at which instability may form, it modifies the wave number of the most unstable mode and also enlarges significantly the range of unstable wave numbers.

Furthermore, by solving numerically the system defining theoretically the wave bifurcation locus (7), (8), we can quantitatively estimate the wave speed s at the onset of instability as a function of inertial times. From the analysis of the results depicted in Fig. 5, we infer that the values of the inertial times affect directly and indirectly through the variation of B_c the migrating speed at the onset of instability, as it varies from about 0.8 (close to the parabolic limit) to 1.0 (away from it), i.e., hyperbolicity may increase the wave speed up to 30%. To get a validation of these results, we integrate again numerically the governing system (1), (2), (32) over a larger time window $t \in [0, 200]$ and a larger spatial domain $l_D = 200$. We use the parameter set corresponding to the points Q$_1$ and Q$_2$ depicted in Fig. 5 and choose the control parameter B in such a way the distance from the threshold is $\epsilon^2 = 10^{-3}$ in both cases. Then, in order to extract the critical values of angular frequency ω_c and wave number k_c, we perform two fast Fourier Transforms (FFTs) on the variable $u(x, t)$, by fixing either space or time. In detail, in
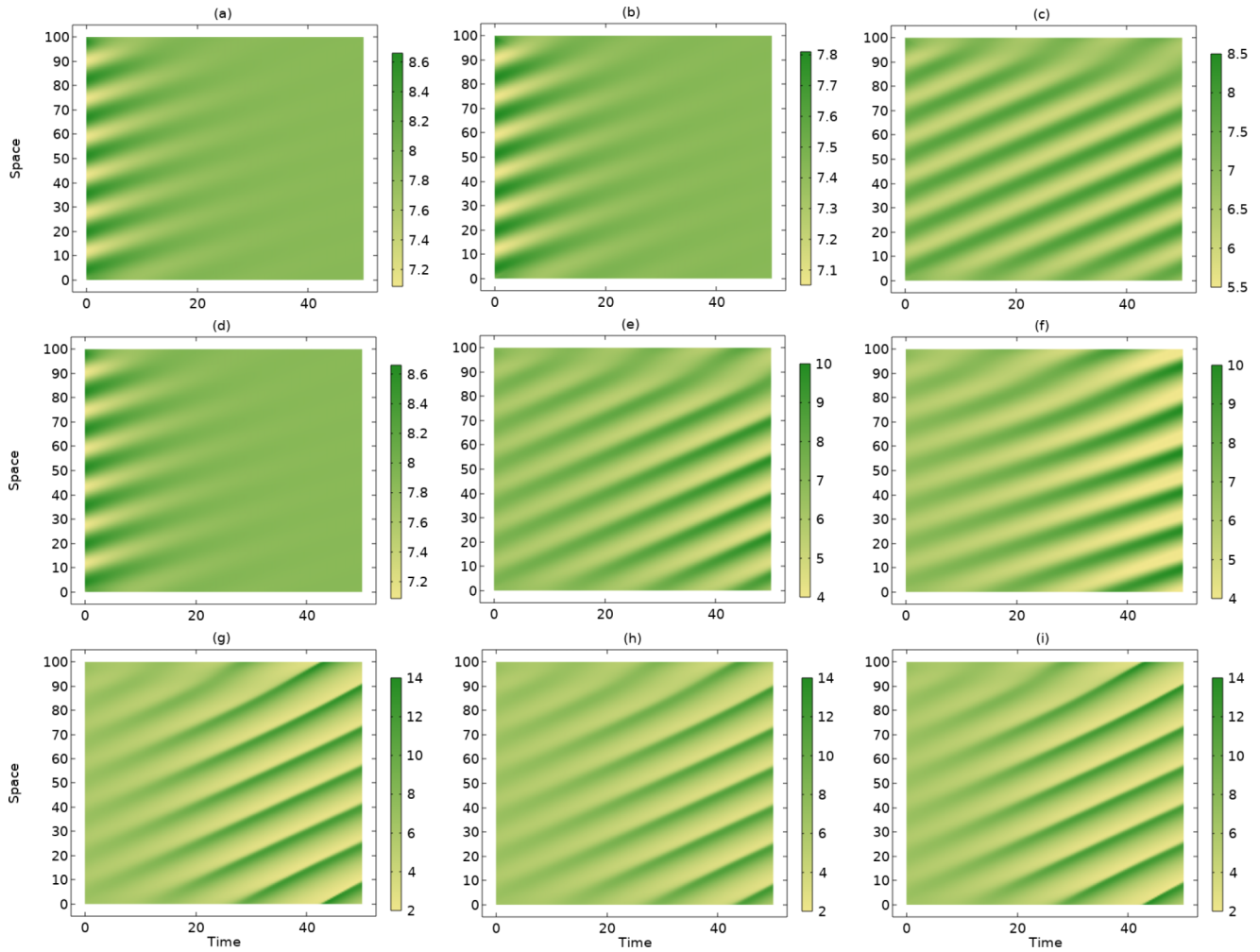
FIG. 3. Spatiotemporal dynamics of vegetation biomass $u(x, t)$ corresponding to the panels shown in Fig. 2 obtained via numerical integration of system (1), (2), (32).
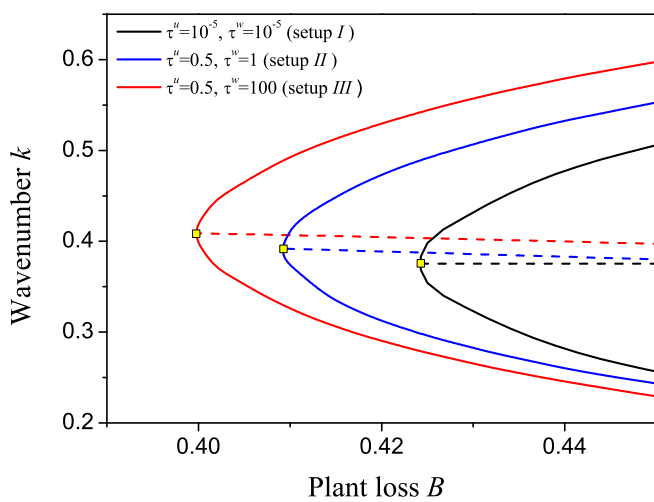

FIG. 4. (Solid lines) Range of unstable wave numbers as a function of the plant loss B for different values of inertial times. (Dashed lines) The wave number of the perturbation with the larger growth rate. (Squares) The lowest plant loss value B_c at which that steady state $\mathbf{U}_S^*$ undergoes wave instability and that identifies the critical wave number k_c.
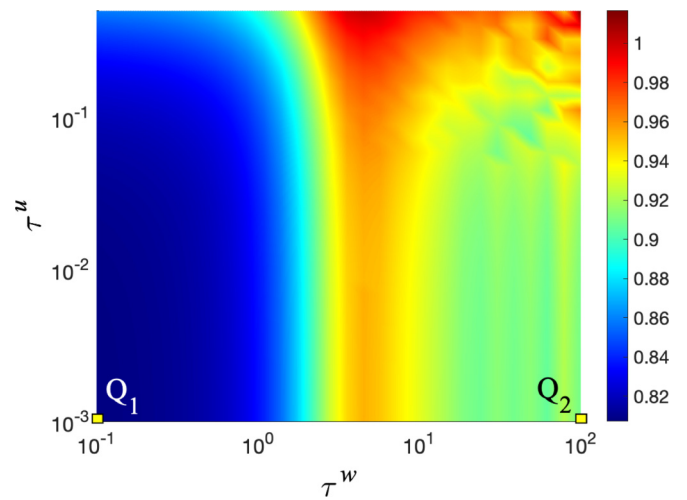
FIG. 5. Density plot of migrating speed s at onset of instability ($B = B_c$) as a function of the inertial times τ^u and τ^w. Fixed parameters: $\nu = 182.5$, $d = 100$, $A = 2.8$.
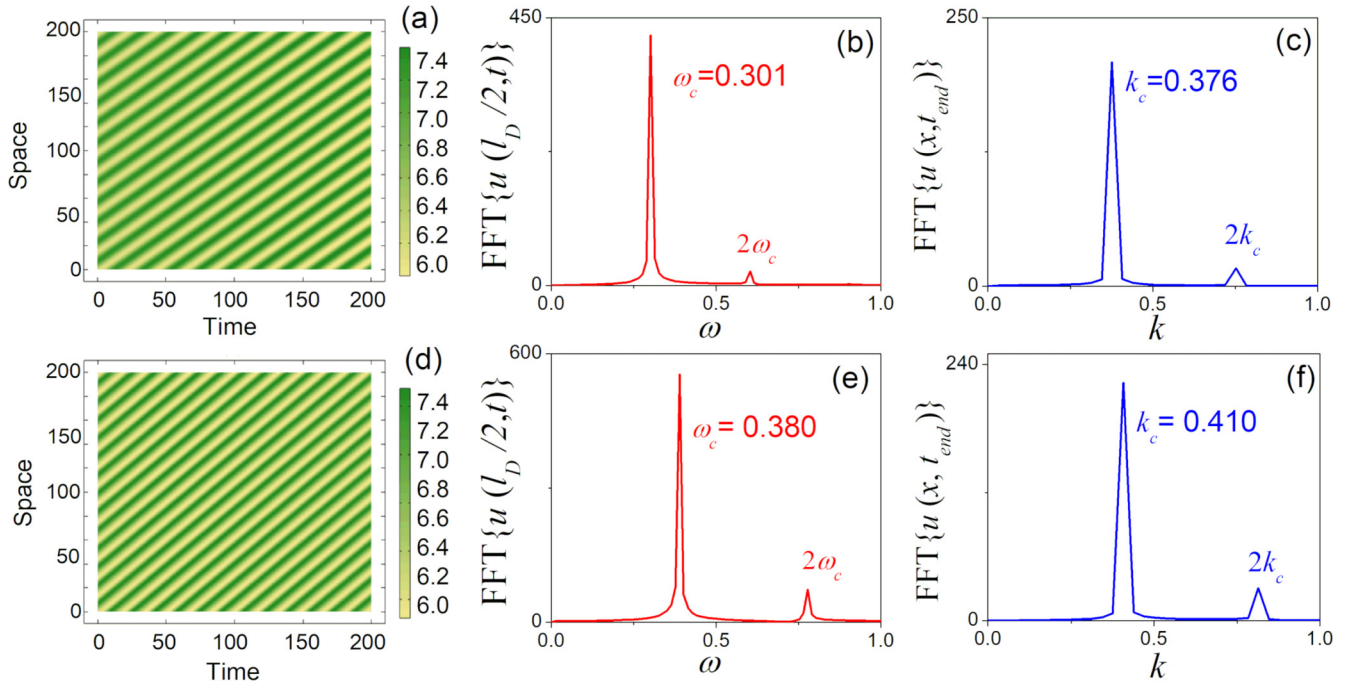
FIG. 6. (a), (d) Snapshots of migrating vegetation patterns. (b), (e) FFT of the *time*-dependent solution evaluated at a fixed location within the domain $u(l_D/2, t)$. (c), (f) FFT of the *space*-dependent solution evaluated at the final simulation time $u(x, t_{end})$. Panels in the top (bottom) row are obtained by using the parameter set corresponding to point Q_1 (Q_2) depicted in Fig. 5. Note that the arising FFT spectra contain some higher-order harmonics [mainly, the component proportional to $\exp(2ik_c z)$] due to the slow modulation of the pattern close to the onset [19].

the former case, the solution $u(x, t)$ is evaluated at $x = l_D/2$ while, in the latter case, it is set at $t = t_{end}$. According to the results shown in Fig. 6, each resulting spectrum contains several peaks, the dominant of which gives information on the angular frequency ω_c and the wave number k_c of the main mode, respectively. Finally, the migrating speed value is simply given by the ratio $s = \omega_c/k_c$. Following this procedure, we get for the point Q_1, $s = 0.301/0.376 = 0.801$, in excellent agreement with the value extracted from system (7), (8), that is equal to $s = 0.807$; for the point Q_2, the value $s = 0.380/0.410 = 0.926$, in good agreement with the theoretical value $s = 0.923$. These results reinforce our previous conclusion on the non-negligible role played by inertial times: apart from affecting the migrating speed, they also alter both angular frequency and wave number of the emerging pattern.

So far, we have validated all the theoretical predictions connected to LSA developed in Sec. II A. Let us now focus on those arising from multiple-scale WNA whose general formulation has been given in Sec. II B. In the specific case of the hyperbolic extension of the Klausmeier model, the explicit expressions of the quantities here involved are reported in Appendix B.

As known, the sign of the real part of the Landau coefficient determines the supercritical (if $L_1 > 0$) or subcritical (if $L_1 < 0$) character of the generated patterns. Here, we aim at inspecting how such a character could be altered by a suitable combination of inertial times. In Fig. 7 we have addressed numerically this investigation, by using the same set of parameters as those used to build Fig. 5. In the figure, the colored (white) areas denote a supercritical (subcritical) behavior. These results reveal that, for relatively small values

of the inertial times, namely, close to the parabolic limit (bottom left corner of the figure), patterns exhibit a supercritical behavior. For increasing values of inertial times, hyperbolicity may give rise to a subcritical instability.

Let us now inspect whether these predictions may be corroborated by numerical simulations. First, the supercritical character associated to the points Q_1 and Q_2 can be extracted from Fig. 6, where patterns slightly above threshold exhibit small amplitude, do not exist for subthreshold values of the
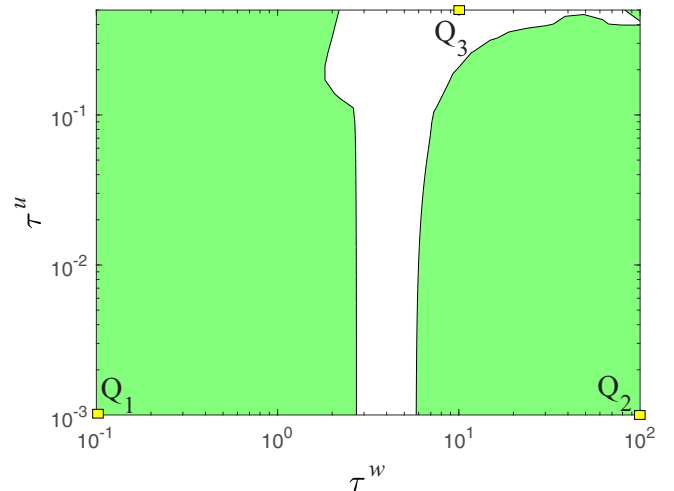

FIG. 7. Contour plot of L_1 as a function of the inertial times τ^u and τ^w. Colored (white) areas denote positive (negative) values of L_1. The parameter set is the same as the one reported in Fig. 5.
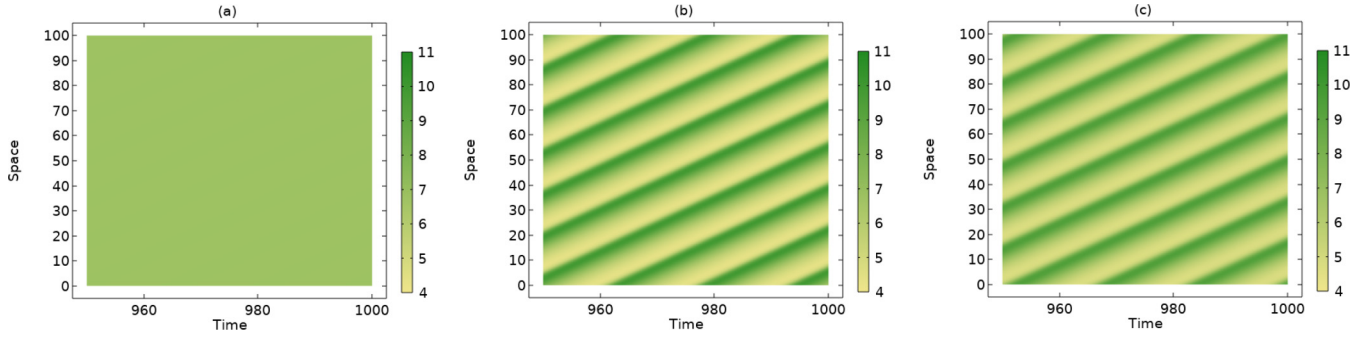
FIG. 8. Snapshots of spatiotemporal evolution of vegetation biomass corresponding to the point Q_3 shown in Fig. 7 for (a) $B = 0.403$, (b) $B = 0.405$, and (c) $B = 0.403$. The initial condition in simulations (a) and (b) is taken as a small periodic perturbation of the steady state $\mathbf{U}_S^*$ whereas in (c) it is given by the final state of (b). The critical value of the control parameter is $B_c = 0.404$.

control parameter, and have a wave number very close to k_c. Indeed, the numerically deduced values, i.e., $k_c = 0.376$ in Fig. 6(c) and $k_c = 0.410$ in Fig. 6(f), are in close agreement with the theoretical ones deduced from (7), (8), (B2), i.e., $k_c = 0.376$ and 0.403, respectively. To test whether a subcritical instability takes place at Q_3, we perform simulations where the initial condition is set, at first, as a small sinusoidal perturbation of the steady state and the control parameter is slightly smaller than the critical value. Results indicate that the initial perturbation simply dies out and the system converges towards the stable homogeneously vegetated area [see Fig. 8(a)]. Then, we increase the control parameter slightly above threshold and, as expected, large amplitude patterns are generated [see Fig. 8(b)] [notice the larger scale in the color bar in comparison with those of Figs. 6(a) and 6(d)]. Finally, we take the final state of this latter simulation as the initial condition of a new simulation where the control parameter is set to the same below-threshold value as the one used to build Fig. 8(a). Interestingly, patterns still survive, so denoting the hysteretic behavior typical of a subcritical instability.

Finally, we investigate on the one-parameter family of coherent structures, solutions of the CCGL equation, and address again a comparison between the analytical predictions reported in Sec. II B 1 and numerical simulations. We shall limit the discussion to the supercritical regime by considering those regions of the (τ^w, τ^u) plane where the real part of the Landau coefficient keeps positive (colored areas in Fig. 7). Then, we study the sign of the necessary condition for stability given by the Benjamin-Feir-Newell criterion (31) and report the results in Fig. 9. Here, the white (orange) color denotes an area where patterns are unstable (may be stable). Our results indicate that, in a wide region enclosing the parabolic limit (point Q_1), i.e., for $\tau^w < 2$ and independently of the value of τ^u, the above-mentioned criterion is always satisfied and patterns may be stable. In this region, a slow modulation of traveling patterns is observed, as shown in Fig. 10(a). Far away from the parabolic limit, there exist values of inertial times that may lead to destabilization of patterns, as it happens in the subregion of the (τ^w, τ^u) plane depicted in Fig. 9. Indeed, considering the inertial times corresponding to point Q_4, the wave-train structure may break up into a sequence of unequal pulses [5], as depicted in Fig. 10(b).

Then, we inspect the role of inertial effects on phase-winding solutions, i.e., on the fixed points $\mathbf{F}_1^*$ and $\mathbf{F}_2^*$ of system

(24). In this analysis, we set the inertial times in such a way they correspond to points Q_1 and Q_2 and keep the dimensionless distance from the threshold fixed at $\epsilon^2 = 10^{-2}$. We integrate the governing system (1), (2), (32) over a larger time window $t \in [0, 1000]$ in order to allow transient regime to expire and the system to reach a steady traveling patterned configuration. These are depicted in Figs. 11(a) and 11(b) by solid lines. To determine the extra parameter involved in the phase-winding solution $\widetilde{\kappa}$, we compare the theoretical critical value k_c with the total wave number of the observed pattern k_{tot}. This value is then used in (25) and (28) to compute the amplitude $\widetilde{Q}$ and the second-order correction of the angular frequency $\widetilde{\omega}$, respectively. Then, the corresponding analytical phase-winding solutions are built via (26). Results are represented in the previously mentioned figures via dashed lines and reveal a satisfying agreement with those arising from numerical simulations. Moreover, we integrate system (24) to describe the heteroclinic orbits joining the fixed points $\mathbf{F}_1^*$ (unstable) and $\mathbf{F}_2^*$ (stable) in the two configurations represented by the points Q_1 and Q_2. The initial condition is set as a small perturbation of $\mathbf{F}_1^*$ in both cases. The resulting fronts are depicted in Fig. 11(c) and confirm that inertial effects take
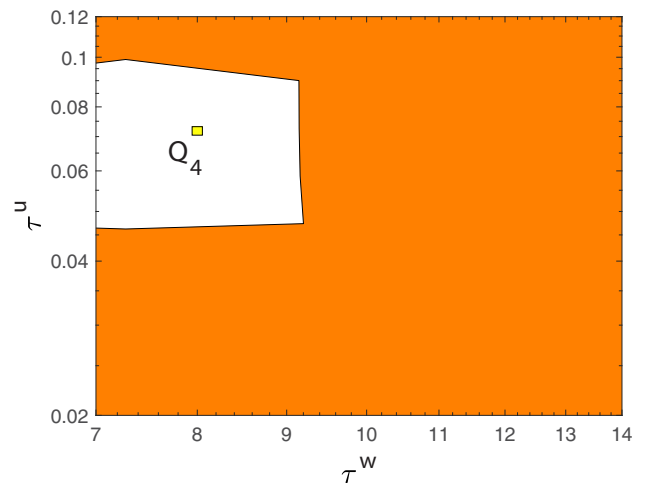

FIG. 9. Plot of the Benjamin-Feir-Newell necessary condition for stability in the supercritical regime. Colored (white) areas denote regions where the condition (31) is (is not) fulfilled.
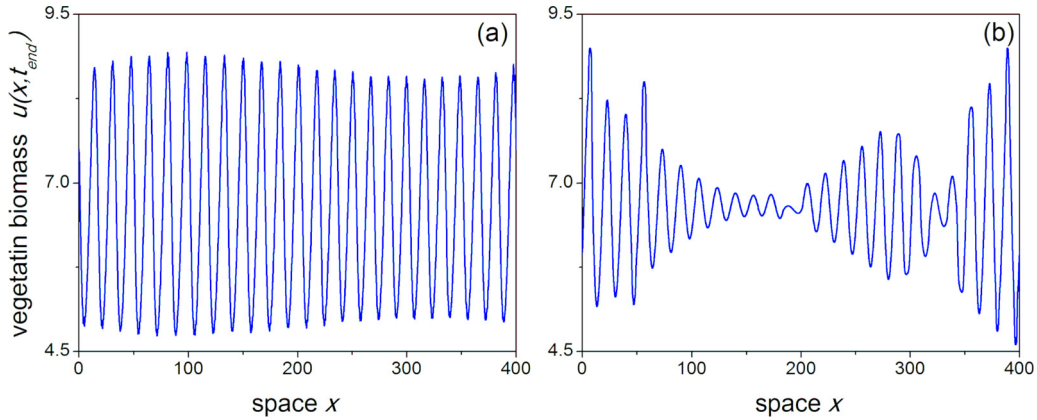
FIG. 10. Proof of the Benjamin-Feir-Newell instability condition showing the spatial profiles of the patterned configurations obtained at points Q_1 (a) and Q_4 (b) represented in Fig. 9(a). To improve the visibility of the wave-train structure breaking, the computational domain has been enlarged to $l_D = 400$.

a relevant role, not only in modulating the duration of the transient regime from the homogeneous steady state to the patterned state, but also in modifying the amplitude, the wave number, and the angular frequency of the traveling patterns.

IV. CONCLUSIONS

In this paper, we have considered a class of hyperbolic reaction-advection-diffusion system for two species, one of which undergoes both diffusion and advection while the other one has a diffusive character only. The hyperbolic structure of the model accounts for the biological inertia of both the involved species and allows a better description of transient phenomena characterized by waves evolving in space over a finite time. On this general framework, we have carried out, first, linear stability analysis to deduce the conditions under which wave instability, responsible for the occurrence of nonstationary spatial patterns, takes place. Then, by applying multiple-scale weakly nonlinear analysis we have determined the amplitude equation describing the slow modulation in space and time near criticality.

All our theoretical findings enclose the parabolic limit as particular case, when the inertial times tend to zero. In particular, it has been shown that the resulting CCGL equation is formally unchanged with respect to the classical one obtained

in parabolic framework, but the coefficients here involved exhibit a strong dependence on inertial times.

Moreover, to better emphasize the role of hyperbolicity, we have also inspected coherent structures of the CCGL equation whose fixed points are in the form of phase-winding solutions. For this class of solutions we have determined the expressions of the key features and established the necessary condition for stability.

The previous theoretical predictions have been tested on an illustrative example, the extended Klausmeier model, describing the formation and the migration of vegetation patterns over a sloping semiarid terrain. Numerical investigations have validated our findings and have allowed to draw several conclusions about the role played by inertia. It has been indeed proven that inertial times do the following:

(1) Enlarge both the wave instability region in the parameter plane where traveling patterns may be observed and is less selective on the range of unstable wave numbers. Thus, inertia allows to destabilize the spatially homogeneous steady state over a wider set of model parameters (see Figs. 1–4).

(2) Vary the key features associated to migrating patterns, speed, wavelength, and angular frequency, leaving all the other model parameters unchanged (see Figs. 5 and 6).

(3) Affect the supercritical or subcritical nature of patterns at onset (see Figs. 7 and 8).
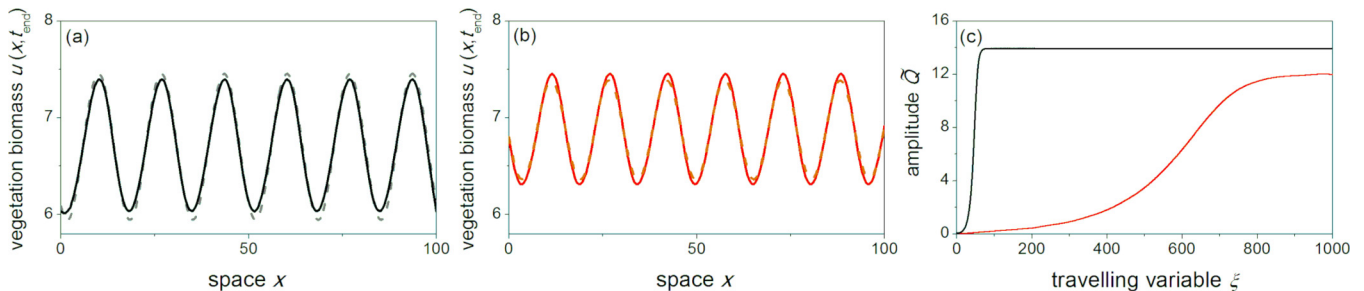

FIG. 11. (a), (b) Comparison between the numerical simulation arising from integration of the governing system (1), (2), (32) (solid lines) and the analytically deduced phase-winding solution $\overline{\mathbf{U}} = \varepsilon \overline{\mathbf{U}}_1$ together with (20) and (25)–(28) (dashed lines). The set of parameters correspond to the points Q_1 (a) and Q_2 (b) with $\epsilon^2 = 10^{-2}$. (c) Results of numerical integration of system (24) representative of the heteroclinic orbits joining the fixed points $\mathbf{F}_1^*$ and $\mathbf{F}_2^*$ [black (red) curve stands for dynamics around point Q_1 (Q_2)]. The initial condition is set as a small perturbation of $\mathbf{F}_1^*$.

(4) Exert influence on localized coherent structures, and in particular on the fronts connecting the plane-wave state to the unstable spatially homogeneous steady state. In particular, it has been shown that inertia takes a role, not only during transient regime, but also modifies the amplitude, the wave number, the angular frequency, and the stability of the phase-winding solution associated to the plane wave (see Figs. 9 and 11).

In the light of the above statements, it has to be emphasized that hyperbolic models provide additional degrees of freedom that can be used to better modeling experimental observations. We plan to extend our hyperbolic framework to the case in which both species undergo diffusion and advection, so enabling the possibility of exploring an even richer set of dynamics.

APPENDIX A: WAVE INSTABILITY IN PARABOLIC REACTION-ADVECTION-DIFFUSION MODELS

In this Appendix we give some details on the occurrence of wave instability in *parabolic* reaction-advection-diffusion models. In this framework, diffusion occurs through Fick's laws, $J^u = -u_x$ and $J^w = -dw_x$, and the governing system is cast as

$$\widetilde{\mathbf{U}}_t + \widetilde{M}\widetilde{\mathbf{U}}_x + D\widetilde{\mathbf{U}}_{xx} = \widetilde{\mathbf{N}}(\widetilde{\mathbf{U}}), \tag{A1}$$

with

$$\widetilde{\mathbf{U}} = \begin{bmatrix} u \\ w \end{bmatrix}, \quad \widetilde{M} = \begin{bmatrix} 0 & 0 \\ 0 & -v \end{bmatrix}, \quad D = \begin{bmatrix} -1 & 0 \\ 0 & -d \end{bmatrix}, \quad \widetilde{\mathbf{N}}(\widetilde{\mathbf{U}}) = \begin{bmatrix} f(u, w) \\ g(u, w) \end{bmatrix}. \tag{A2}$$

The resulting spatially homogeneous steady states are denoted by $\widetilde{\mathbf{U}}^* = (u^*, v^*)$ and the dispersion relation reduces to a quadratic equation

$$\omega^2 + \left[k^2(d+1) - (f_u^* + g_w^*) - ikv \right]\omega + \widetilde{A}_0 + ikv\widehat{b}_0 = 0 \tag{A3}$$

with $\widetilde{A}_0$ and $\widehat{b}_0$ given in (4). Conditions (6) for the stability of $\widetilde{\mathbf{U}}^*$ against homogeneous perturbations hold for both hyperbolic and parabolic models.

By applying the same procedure as the one discussed in Sec. II A in the hyperbolic framework, but exploiting the lower complexity of the characteristic equation (A3) with respect to (3), the locus of wave instability can be defined implicitly via the following equation:

$$(4\chi_2^3 + 2\chi_0\chi_2 + \chi_1)(4\chi_2^3 + 2\chi_0\chi_2 - \chi_1) = 0, \tag{A4}$$

whereas the critical wave number is given by

$$k_c^2 = -\frac{\chi_3}{\chi_4} \pm \chi_2 \tag{A5}$$

and the wave speed obeys

$$s = v(f_u^* - k_c^2) \Big/ \left[k_c^2(d+1) - f_u^* - g_w^* \right]. \tag{A6}$$

The expressions of the coefficients χ_i $(i = 0, \ldots, 4)$ appearing in (A4) and (A5) are given by

$$\chi_0 = \frac{8\chi_4\chi_8 - 3\chi_3^2}{8\chi_4^2}, \quad \chi_1 = \frac{8\chi_4^2\chi_9 - 4\chi_4\chi_3\chi_8 + \chi_3^3}{8\chi_4^3}, \quad \chi_2 = \frac{1}{2}\sqrt{-\frac{2}{3}\chi_0 + \frac{1}{3\chi_4}\left(\chi_5 + \frac{\chi_6}{\chi_5}\right)},$$

$$\chi_3 = dv^2 - (d+1)^2(g_w^* + df_u^*) - 2d(d+1)(f_u^* + g_w^*), \quad \chi_4 = d(d+1)^2, \tag{A7}$$

where

$$\chi_5 = \sqrt[3]{\frac{\chi_7 + \sqrt{\chi_7^2 - 4\chi_6^3}}{2}}, \quad \chi_6 = 12\chi_4\chi_{10} - 3\chi_3\chi_9 + \chi_8^2,$$

$$\chi_7 = 27\chi_4\chi_9^2 - 72\chi_4\chi_8\chi_{10} + 27\chi_3^2\chi_{10} - 9\chi_3\chi_8\chi_9 + 2\chi_8^3,$$

$$\chi_8 = d(f_u^* + g_w^*)^2 + 2(d+1)(f_u^* + g_w^* - v^2)(g_w^* + df_u^*) + (d+1)^2(f_u^*g_w^* + f_w^*g_u^*),$$

$$\chi_9 = v^2 f_u^* g_w^* - (g_w^* + df_u^*)(f_u^* + g_w^*)^2 - 2(d+1)(f_u^* + g_w^*)(f_u^*g_w^* + f_w^*g_u^*),$$

$$\chi_{10} = (f_u^* + g_w^*)^2(f_u^*g_w^* + f_w^*g_u^*). \tag{A8}$$

Note that, in the parabolic case, the critical value of the control parameter B_c is defined implicitly by the sole highly nonlinear equation (A4), which results to be decoupled from the others. Moreover, the sign in (A5) has to be chosen in such a way it gives real and positive values for B_c and k_c.

APPENDIX B: DERIVATION OF CUBIC COMPLEX GINZURG-LANDAU EQUATION

In this Appendix we fully describe the procedure to deduce the CCGL Eq. (22) for the hyperbolic reaction-advection-diffusion model (1), (2).

First of all, substituting the expansion (14) into the governing system (9) and looking for solution $\overline{\mathbf{U}}_i = \overline{\mathbf{U}}_i(z)$ with $z = x - st$, the set of ordinary differential equations (16)–(18), to be solved sequentially, is obtained. At the first perturbative order, the system reads as

$$\frac{d\overline{\mathbf{U}}_1}{dz} = K_c^* \overline{\mathbf{U}}_1, \tag{B1}$$

where the matrix K_c^*, defined in (19), admits four complex eigenvalues given by

$$\lambda_{1,2} = \mp i k_c \quad \text{with} \quad k_c^2 = \left.\frac{\delta_3}{\delta_1}\right|_c \tag{B2}$$

and

$$\lambda_{3,4} = \alpha \mp i\beta \quad \text{with} \quad \alpha = \left.-\frac{\delta_1}{2}\right|_c \quad \text{and} \quad \beta = \left.\sqrt{\left(\frac{\delta_1 \delta_4}{\delta_3} - \frac{\delta_1^2}{4}\right)}\right|_c \tag{B3}$$

to which there correspond the following right eigenvectors:

$$\mathbf{d}^{(\pm i k_c)} = \begin{bmatrix} r_1 \pm i\widehat{r}_1 \\ r_2 \pm i\widehat{r}_2 \\ r_3 \pm i\widehat{r}_3 \\ r_4 \pm i\widehat{r}_4 \end{bmatrix}, \qquad \mathbf{d}^{(\alpha \pm i\beta)} = \begin{bmatrix} y_1 \pm i\widehat{y}_1 \\ y_2 \pm i\widehat{y}_2 \\ y_3 \pm i\widehat{y}_3 \\ y_4 \pm i\widehat{y}_4 \end{bmatrix}. \tag{B4}$$

The general solution of the homogeneous linear system (B1) can be expressed as

$$\mathbf{U}_1 = P e^{Qz} P^{-1} \mathbf{C}(T_2), \tag{B5}$$

where the vector $\mathbf{C}(T_2)$ is determined by boundary conditions, whereas P and Q are, respectively, the eigenvectors and eigenvalues matrices of K_c^* given by

$$P = \begin{bmatrix} r_1 + i\widehat{r}_1 & r_1 - i\widehat{r}_1 & y_1 + i\widehat{y}_1 & y_1 - i\widehat{y}_1 \\ r_2 + i\widehat{r}_2 & r_2 - i\widehat{r}_2 & y_2 + i\widehat{y}_2 & y_2 - i\widehat{y}_2 \\ r_3 + i\widehat{r}_3 & r_3 - i\widehat{r}_3 & y_3 + i\widehat{y}_3 & y_3 - i\widehat{y}_3 \\ r_4 + i\widehat{r}_4 & r_4 - i\widehat{r}_4 & y_4 + i\widehat{y}_4 & y_4 - i\widehat{y}_4 \end{bmatrix}, \quad Q = \begin{bmatrix} ik_c & 0 & 0 & 0 \\ 0 & -ik_c & 0 & 0 \\ 0 & 0 & \alpha + i\beta & 0 \\ 0 & 0 & 0 & \alpha - i\beta \end{bmatrix}. \tag{B6}$$

Then, solution of (B1) reads as

$$\overline{\mathbf{U}}_1 = \Omega(X, T_2) e^{ik_c z} \mathbf{d}^{(ik_c)} + \overline{\Omega}(X, T_2) e^{-ik_c z} \mathbf{d}^{(-ik_c)}, \tag{B7}$$

where the complex pattern amplitude Ω remains undetermined at this stage and $\overline{\Omega}$ denotes its complex conjugate.

At the second order, the governing system is the following:

$$\frac{d\overline{\mathbf{U}}_2}{dz} - K_c^* \overline{\mathbf{U}}_2 = (M - sI)^{-1} \left\{ \frac{1}{2} (\overline{\mathbf{U}}_1 \cdot \nabla)^{(2)} \mathbf{N}|_c^* - M \frac{\partial \overline{\mathbf{U}}_1}{\partial X} \right\} \tag{B8}$$

whose general solution is given by

$$\mathbf{U}_2 = P e^{Qz} P^{-1} \mathbf{C}(T_2) + P e^{Qz} \int e^{-Qz} (MP)^{-1} \mathbf{F} \, dz, \tag{B9}$$

where $\mathbf{F}$ is the nonhomogeneous term at the right-hand side of (B8).

Now, taking into account (B9) and inserting (B7) into the nonhomogeneous linear system (B8), the solution at the second perturbative order satisfying periodic boundary conditions reads as

$$\overline{\mathbf{U}}_2 = \frac{\partial \Omega}{\partial X} e^{ik_c z} \mathbf{g} + \frac{\partial \overline{\Omega}}{\partial X} e^{-ik_c z} \overline{\mathbf{g}} + \Omega^2 e^{2ik_c z} \mathbf{q} + \overline{\Omega}^2 e^{-2ik_c z} \overline{\mathbf{q}} + 2\mathbf{q}_0 |\Omega|^2, \tag{B10}$$

where the vectors

$$\mathbf{g} = \begin{bmatrix} g_1 + i\widehat{g}_1 \\ g_2 + i\widehat{g}_2 \\ g_3 + i\widehat{g}_3 \\ g_4 + i\widehat{g}_4 \end{bmatrix}, \quad \mathbf{q} = \begin{bmatrix} q_1 + i\widehat{q}_1 \\ q_2 + i\widehat{q}_2 \\ q_3 + i\widehat{q}_3 \\ q_4 + i\widehat{q}_4 \end{bmatrix}, \quad \mathbf{q}_0 = \begin{bmatrix} q_{01} \\ q_{02} \\ 0 \\ 0 \end{bmatrix} \tag{B11}$$

fulfill the linear systems

$$[L_c^* - ik_c(M - sI)]\mathbf{g} = M\mathbf{d}^{(ik_c)},$$

$$[L_c^* - 2ik_c(M - sI)]\mathbf{q} = -\tfrac{1}{2}(\mathbf{d}^{(ik_c)} \cdot \nabla)^{(2)}\mathbf{N}|_c^*,$$

$$L_c^*\mathbf{q}_0 = -\tfrac{1}{2}(\mathbf{d}^{(ik_c)} \cdot \nabla)(\mathbf{d}^{(-ik_c)} \cdot \nabla)\mathbf{N}|_c^* \tag{B12}$$

with

$$\mathbf{l}M\mathbf{d}^{(ik_c)} = \mathbf{0},$$

$$\mathbf{l}[L_c^* - ik_c(M - sI)] = \mathbf{0}, \tag{B13}$$

whereas $\overline{\mathbf{g}}$ and $\overline{\mathbf{q}}$ are the complex conjugate of $\mathbf{g}$ and $\mathbf{q}$, respectively.

Finally, by substituting (B7) and (B10) into (18), from the removal of secular terms, we deduce that the pattern amplitude $\Omega(X, T_2)$ satisfies the CCGL equation

$$\frac{\partial \Omega}{\partial T_2} = (\rho_1 + i\rho_2)\frac{\partial^2 \Omega}{\partial X^2} + (\sigma_1 + i\sigma_2)\Omega - (L_1 - iL_2)\Omega\,|\Omega|^2, \tag{B14}$$

where:

$$\rho_1 + i\rho_2 = [(n_1e_1 + n_2e_2) + i(n_2e_1 - n_1e_2)]/(e_1^2 + e_2^2),$$

$$\sigma_1 + i\sigma_2 = B_2[(m_1e_1 + m_2e_2) + i(m_2e_1 - m_1e_2)]/(e_1^2 + e_2^2),$$

$$L_1 - iL_2 = (p_1 - ip_2)/(e_1^2 + e_2^2) \tag{B15}$$

with

$$n_1 = [(g_4 - vg_2)f_u^* - g_3g_u^*]E_{1r} + [(g_4 - vg_2)f_w^* - g_3g_w^*]E_{2r} + (f_u^*g_w^* - f_w^*g_u^*)(dg_2E_{4r} - g_1E_{3r}),$$

$$n_2 = [(g_4 - vg_2)f_u^* - g_3g_u^*]E_{1i} + [(g_4 - vg_2)f_w^* - g_3g_w^*]E_{2i} + (f_u^*g_w^* - f_w^*g_u^*)(dg_2E_{4i} - g_1E_{3i}),$$

$$m_1 = -(s_1r_1 + s_2r_2)(E_{1r}f_u^* + E_{2r}f_w^*) + (s_1\widehat{r}_1 + s_2\widehat{r}_2)(E_{1i}f_u^* + E_{2i}f_w^*)$$
$$\quad + (h_1r_1 + h_2r_2)(E_{1r}g_u^* + E_{2r}g_w^*) - (h_1\widehat{r}_1 + h_2\widehat{r}_2)(E_{1i}g_u^* + E_{2i}g_w^*),$$

$$m_2 = -(s_1r_1 + s_2r_2)(E_{1i}f_u^* + E_{2i}f_w^*) - (s_1\widehat{r}_1 + s_2\widehat{r}_2)(E_{1r}f_u^* + E_{2r}f_w^*)$$
$$\quad + (h_1r_1 + h_2r_2)(E_{1i}g_u^* + E_{2i}g_w^*) + (h_1\widehat{r}_1 + h_2\widehat{r}_2)(E_{1r}g_u^* + E_{2r}g_w^*),$$

$$p_1 = (b_1f_u^* - a_1g_u^*)(E_{1r}e_1 + E_{1i}e_2) - (b_2f_u^* - a_2g_u^*)(E_{1i}e_1 - E_{1r}e_2)$$
$$\quad + (b_1f_w^* - a_1g_w^*)(E_{2r}e_1 + E_{2i}e_2) - (b_2f_w^* - a_2g_w^*)(E_{2i}e_1 - E_{2r}e_2),$$

$$p_2 = (b_1f_u^* - a_1g_u^*)(E_{1i}e_1 - E_{1r}e_2) - (b_2f_u^* - a_2g_u^*)(E_{1r}e_1 + E_{1i}e_2)$$
$$\quad + (b_1f_w^* - a_1g_w^*)(E_{2i}e_1 - E_{2r}e_2) - (b_2f_w^* - a_2g_w^*)(E_{2r}e_1 + E_{2i}e_2),$$

$$e_1 = (r_1g_u^* - r_2f_u^*)E_{1r} - (\widehat{r}_1g_u^* - \widehat{r}_2f_u^*)E_{1i} + (r_1g_w^* - r_2f_w^*)E_{2r} - (\widehat{r}_1g_w^* - \widehat{r}_2f_w^*)E_{2i}$$
$$\quad + (f_u^*g_w^* - f_w^*g_u^*)(\tau^ur_3E_{3r} - \tau^wr_4E_{4r} - \tau^u\widehat{r}_3E_{3i} + \tau^w\widehat{r}_4E_{4i}),$$

$$e_2 = (r_1g_u^* - r_2f_u^*)E_{1i} + (\widehat{r}_1g_u^* - \widehat{r}_2f_u^*)E_{1r} + (r_1g_w^* - r_2f_w^*)E_{2i} + (\widehat{r}_1g_w^* - \widehat{r}_2f_w^*)E_{2r}$$
$$\quad + (f_u^*g_w^* - f_w^*g_u^*)(\tau^ur_3E_{3i} - \tau^wr_4E_{4i} + \tau^u\widehat{r}_3E_{3r} - \tau^w\widehat{r}_4E_{4r}),$$

$$E_{1r} + iE_{1i} = \widehat{r}_4(y_1\widehat{y}_3 - y_3\widehat{y}_1) + \widehat{r}_3(y_4\widehat{y}_1 - y_1\widehat{y}_4) + \widehat{r}_1(y_3\widehat{y}_4 - y_4\widehat{y}_3)$$
$$\quad + i[r_4(y_1\widehat{y}_3 - y_3\widehat{y}_1) + r_3(y_4\widehat{y}_1 - y_1\widehat{y}_4) + r_1(y_3\widehat{y}_4 - y_4\widehat{y}_3)],$$

$$E_{2r} + iE_{2i} = \widehat{r}_4(y_2\widehat{y}_3 - y_3\widehat{y}_2) + \widehat{r}_3(y_4\widehat{y}_2 - y_2\widehat{y}_4) + \widehat{r}_2(y_3\widehat{y}_4 - y_4\widehat{y}_3)$$
$$\quad + i[r_4(y_2\widehat{y}_3 - y_3\widehat{y}_2) + r_3(y_4\widehat{y}_2 - y_2\widehat{y}_4) + r_2(y_3\widehat{y}_4 - y_4\widehat{y}_3)],$$

$$E_{3r} + iE_{3i} = \widehat{r}_4(y_2\widehat{y}_1 - y_1\widehat{y}_2) + \widehat{r}_2(y_1\widehat{y}_4 - y_4\widehat{y}_1) + \widehat{r}_1(y_4\widehat{y}_2 - y_2\widehat{y}_4)$$
$$\quad + i[r_4(y_2\widehat{y}_1 - y_1\widehat{y}_2) + r_2(y_1\widehat{y}_4 - y_4\widehat{y}_1) + r_1(y_4\widehat{y}_2 - y_2\widehat{y}_4)],$$

$$E_{4r} + iE_{4i} = \widehat{r}_3(y_2\widehat{y}_1 - y_1\widehat{y}_2) + \widehat{r}_2(y_1\widehat{y}_3 - y_3\widehat{y}_1) + \widehat{r}_1(y_3\widehat{y}_2 - y_2\widehat{y}_3)$$
$$\quad + i[r_3(y_2\widehat{y}_1 - y_1\widehat{y}_2) + r_2(y_1\widehat{y}_3 - y_3\widehat{y}_1) + r_1(y_3\widehat{y}_2 - y_2\widehat{y}_3)], \tag{B16}$$

$$h_1 = \frac{df_u}{dB}\Big|_c^*, \quad h_2 = \frac{df_w}{t\,dB}\Big|_c^*, \quad s_1 = \frac{dg_u}{dB}\Big|_c^*, \quad s_2 = \frac{dg_w}{dB}\Big|_c^*,$$

and

$$
\begin{aligned}
a_1 + ia_2 =\ & f_{uu}|_c^*\{r_1(2q_{01}+q_1)+\widehat{r_1}\widehat{q_1}+i[\widehat{r_1}(2q_{01}-q_1)+r_1\widehat{q_1}]\} \\
& + f_{uw}|_c^*\{r_1(2q_{02}+q_2)+\widehat{r_1}\widehat{q_2}+r_2(2q_{01}+q_1)+\widehat{r_2}\widehat{q_1}+i[\widehat{r_1}(2q_{02}-q_2)+r_1\widehat{q_2}+\widehat{r_2}(2q_{01}-q_1)+r_2\widehat{q_1}]\} \\
& + f_{ww}|_c^*\{r_2(2q_{02}+q_2)+\widehat{r_2}\widehat{q_2}+i[\widehat{r_2}(2q_{02}-q_2)+r_2\widehat{q_2}]\} \\
& + \tfrac{1}{2}f_{uuu}\big|_c^*\mathrm{ig}(r_1^2+\widehat{r_1}^2\mathrm{ig})(r_1+i\widehat{r_1}) + \tfrac{1}{2}f_{www}|_c^*(r_2^2+\widehat{r_2}^2)(r_2+i\widehat{r_2}) \\
& + \tfrac{1}{2}f_{uuw}\big|_c^*\{2r_1\widehat{r_1}\widehat{r_2}+r_2\big(3r_1^2+\widehat{r_1}^2\big)+i[2r_1\widehat{r_1}r_2+\widehat{r_2}\big(r_1^2+3\widehat{r_1}^2\big)]\} \\
& + \tfrac{1}{2}f_{uww}\big|_c^*\{2r_2\widehat{r_1}\widehat{r_2}+r_1\big(3r_2^2+\widehat{r_2}^2\big)+i[2r_1\widehat{r_1}r_2+\widehat{r_1}\big(r_2^2+3\widehat{r_2}^2\big)]\}, \\
b_1 + ib_2 =\ & g_{uu}|_c^*\{r_1(2q_{01}+q_1)+\widehat{r_1}\widehat{q_1}+i[\widehat{r_1}(2q_{01}-q_1)+r_1\widehat{q_1}]\} \\
& + g_{uw}|_c^*\{r_1(2q_{02}+q_2)+\widehat{r_1}\widehat{q_2}+r_2(2q_{01}+q_1)+\widehat{r_2}\widehat{q_1} \\
& + i[\widehat{r_1}(2q_{02}-q_2)+r_1\widehat{q_2}+\widehat{r_2}(2q_{01}-q_1)+r_2\widehat{q_1}]\} \\
& + g_{ww}|_c^*\{r_2(2q_{02}+q_2)+\widehat{r_2}\widehat{q_2}+i[\widehat{r_2}(2q_{02}-q_2)+r_2\widehat{q_2}]\} \\
& + \tfrac{1}{2}g_{uuu}\big|_c^*(r_1^2+\widehat{r_1}^2)(r_1+i\widehat{r_1}) + \tfrac{1}{2}(g_{www})|_c^*(r_2^2+\widehat{r_2}^2)(r_2+i\widehat{r_2}) \\
& + \tfrac{1}{2}g_{uuw}\big|_c^*\{2r_1\widehat{r_1}\widehat{r_2}+r_2\big(3r_1^2+\widehat{r_1}^2\big)+i[2r_1\widehat{r_1}r_2+\widehat{r_2}\big(r_1^2+3\widehat{r_1}^2\big)]\} \\
& + \tfrac{1}{2}g_{uww}\big|_c^*\{2r_2\widehat{r_1}\widehat{r_2}+r_1\big(3r_2^2+\widehat{r_2}^2\big)+i[2r_1\widehat{r_1}r_2+\widehat{r_1}\big(r_2^2+3\widehat{r_2}^2\big)]\}.
\end{aligned}
\tag{B17}
$$

In the particular case of the hyperbolic extension of the Klausmeier model, taking into account

$$
\begin{aligned}
& f_u^* = B, \quad f_w^* = u_S^2, \quad g_u^* = -2B, \quad g_w^* = -\big(1+u_S^2\big), \\
& f_{uu}^* = 2B/u_S, \quad f_{uw}^* = 2u_S, \quad f_{ww}^* = 0, \\
& g_{uu}^* = -2B/u_S, \quad g_{uw}^* = -2u_S, \quad g_{ww}^* = 0, \\
& f_{uuu}^* = f_{uww}^* = f_{www}^* = 0, \quad f_{uuw}^* = 2, \\
& g_{uuu}^* = g_{uww}^* = g_{www}^* = 0, \quad g_{uuw}^* = -2,
\end{aligned}
\tag{B18}
$$

the components of the right eigenvectors $\mathbf{d}^{(\pm ik_c)}$ and $\mathbf{d}^{(\alpha\pm i\beta)}$ reported in (B4) become

$$
\begin{aligned}
& r_1 = 1, \widehat{r_1} = 0, \\
& r_2 = \frac{k_c^2 - B_c - (\tau^u)^2 k_c^2 s^2 B_c}{u_{S_c}^2\big[k_c^2 s^2(\tau^u)^2 + 1\big]}, \quad \widehat{r_2} = -\frac{k_c s[1 + k_c^2\tau^u(\tau^u s^2 - 1)]}{u_{S_c}^2\big[k_c^2 s^2(\tau^u)^2 + 1\big]}, \\
& r_3 = \frac{k_c^2 s\tau^u}{k_c^2 s^2(\tau^u)^2 + 1}, \quad \widehat{r_3} = -\frac{k_c}{k_c^2 s^2(\tau^u)^2 + 1}, \\
& r_4 = \frac{k_c d(\widehat{r_2} + k_c s r_2\tau^w)}{1 + (\tau^w)^2 k_c^2 s^2}, \quad \widehat{r_4} = \frac{k_c d(-r_2 + k_c s\widehat{r_2}\tau^w)}{1 + (\tau^w)^2 k_c^2 s^2}, \\
& y_1 = 1, \widehat{y_1} = 0, \\
& y_2 = \frac{(\alpha s\tau^u - 1)l_1 + \beta s\tau^u l_2}{u_{S_c}^2\big[(\alpha s\tau^u - 1)^2 + \beta^2 s^2(\tau^u)^2\big]}, \quad \widehat{y_2} = \frac{(\alpha s\tau^u - 1)l_2 - \beta s\tau^u l_1}{u_{S_c}^2\big[(\alpha s\tau^u - 1)^2 + \beta^2 s^2(\tau^u)^2\big]}, \\
& y_3 = \frac{\alpha(\alpha s\tau^u - 1) + \beta^2 s\tau^u}{(\alpha s\tau^u - 1)^2 + \beta^2 s^2(\tau^u)^2}, \quad \widehat{y_3} = -\frac{\beta}{(\alpha s\tau^u - 1)^2 + \beta^2 s^2(\tau^u)^2}, \\
& y_4 = \frac{d[(\alpha y_2 - \beta\widehat{y_2})(\alpha s\tau^w - 1) + \beta s\tau^w(\beta y_2 + \alpha\widehat{y_2})]}{(\tau^w\alpha s - 1)^2 + \beta^2 s^2(\tau^w)^2}, \quad \widehat{y_4} = \frac{d[(\beta y_2 + \alpha\widehat{y_2})(\alpha s\tau^w - 1) + \beta s\tau^w(\beta\widehat{y_2} - \alpha y_2)]}{(\tau^w\alpha s - 1)^2 + \beta^2 s^2(\tau^w)^2},
\end{aligned}
\tag{B19}
$$

where

$$l_1 = (\alpha^2 - \beta^2)(1 - s^2\tau^u) + \alpha s(1 - B_c\tau^u) + Bc, \quad l_2 = 2\alpha\beta(1 - s^2\tau^u) + \beta s(1 - \tau^u B_c). \quad (B20)$$

Moreover, the coefficients occurring in (B17) reduce to

$$a_1 + ia_2 = 2B_c/u_{Sc}[r_1(2q_{01} + q_1) + \widehat{r_1}\widehat{q_1}] + 2r_1\widehat{r_1}\widehat{r_2} + r_2(3r_1^2 + \widehat{r_1^2}) + 2u_{Sc}[r_1(2q_{02} + q_2) + \widehat{r_1}\widehat{q_2} + r_2(2q_{01} + q_1) + \widehat{r_2}\widehat{q_1}]$$
$$+ i\{2B_c/u_{Sc}[\widehat{r_1}(2q_{01} - q_1) + r_1\widehat{q_1}] + 2r_1\widehat{r_1}r_2 + \widehat{r_2}(r_1^2 + 3\widehat{r_1^2}) + 2u_{Sc}[\widehat{r_1}(2q_{02} - q_2) + r_1\widehat{q_2} + \widehat{r_2}(2q_{01} - q_1) + r_2\widehat{q_1}]\},$$

$$b_1 + ib_2 = -(a_1 + ia_2). \quad (B21)$$

[1] M. C. Cross and P. C. Hohenberg, Pattern formation outside of equilibrium, Rev. Mod. Phys. **65**, 851 (1993).

[2] D. Walgraef, *Spatio-Temporal Pattern Formation* (Springer, New York, 1997).

[3] J. D. Murray, *Mathematical Biology: I. An Introduction* (Springer, New York, 2002).

[4] J. D. Murray, *Mathematical Biology II: Spatial Models and Biomedical Applications* (Springer, Berlin, 2003).

[5] R. Hoyle, *Pattern Formation. An Introduction to Methods* (Cambridge University Press, New York, 2007).

[6] M. Cross and H. Greenside, *Pattern Formation and Dynamics in Nonequilibrium Systems* (Cambridge University Press, Cambridge, 2009).

[7] A. M. Turing, The chemical basis of morphogenesis, Philos. Trans. R. Soc. London, Ser. B **237**, 37 (1952).

[8] E. P. Zemskov and W. Horsthemke, Diffusive instabilities in hyperbolic reaction-diffusion equations, Phys. Rev. E **93**, 032211 (2016).

[9] C. R. Doering, J. D. Gibbon, D. D. Holm, and B. Nicolaenko, Exact Lyapunov Dimension of the Universal Attractor for the Complex Ginzburg-Landau Equation, Phys. Rev. Lett. **59**, 2911 (1987).

[10] C. R. Doering, J. D. Gibbon, D. D. Holm, and B. Nicolaenko, Low-dimensional behaviour in the complex Ginzburg-Landau equation, Nonlinearity **1**, 279 (1988).

[11] A. Van Harten, On the validity of the Ginzburg-Landau equation, J. Nonlinear Sci. **1**, 397 (1991).

[12] G. Schneider, Global existence via Ginzburg-Landau formalism and pseudo-orbits of Ginzburg-Landau approximations, Commun. Math. Phys. **164**, 157 (1994).

[13] A. Doelman, R. Gardner, and C. Jones, Instability of quasiperiodic solutions of the Ginzburg-Landau equation, Proc. R. Soc. Edinburgh: Sect. A: Math. **125**, 501 (1995).

[14] A. Mielke and G. Schneider, *Derivation and Justification of the Complex Ginzburg Landau Equation as a Modulation Equation*, in: P. Deift, C. D. Levermore, and C. E. Wayne, Lecture in Applied Mathematics (American Mathematical Society, Providence, RI, 1994), Vol. 31, pp. 191–216.

[15] C. D. Levermore and D. R. Stark, Inertial ranges for turbulent solutions of complex Ginzburg-Landau equations, Phys. Lett. A **234**, 269 (1997).

[16] I. Melbourne, Derivation of the time-dependent ginzburg-landau equation on the line, J. Nonlinear Sci. **8**, 1 (1998).

[17] A. Mielke, Bounds for the solutions of the complex Ginzburg-Landau equation in terms of the dispersion parameters, Phys. D (Amsterdam) **117**, 106 (1998).

[18] A. Mielke, The Ginzburg-Landau equation in its role as a modulation equation, in: B. Fiedler, *Handbook of Dynamical Systems* (Elsevier, Amsterdam, 2002), Vol. 2, pp. 759–834.

[19] W. van Saarloos and P. C. Hohenberg, Pulses and Fronts in the Complex Ginzburg-Landau Equation near a Subcritical Bifurcation, Phys. Rev. Lett. **64**, 749 (1990).

[20] W. Van Saarloos and P. C. Hohenberg, Fronts, pulses, sources and sinks in generalized complex Ginzburg-Landau equations, Phys. D (Amsterdam) **56**, 303 (1992).

[21] W. Van Saarloos, The complex Ginzburg-Landau equation for beginners, in: P. E. Cladis, P. Palffy-Muhoray, in *Proceedings of the Santa Fe Workshop on "Spatio-Temporal Patterns in Nonequilibrium Complex Systems"* (Addison-Wesley, Chicago, 1994).

[22] L. Brusch, A. Torcini, M. Van Hecke, M. G. Zimmermann, and M. Bar, Modulated amplitude waves and defect formation in the one-dimensional complex Ginzburg-Landau equation, Phys. D (Amsterdam) **160**, 127 (2001).

[23] I. S. Aranson and L. Kramer, The world of the complex Ginzburg-Landau equation, Rev. Mod. Phys. **74**, 99 (2002).

[24] G. Consolo, C. Curró, and G. Valenti, Pattern formation and modulation in a hyperbolic vegetation model for semiarid environments, Appl. Math. Model. **43**, 372 (2017).

[25] C. Curró and G. Valenti, Pattern formation in hyperbolic models with cross-diffusion: Theory and applications, Phys. D (Amsterdam) **418**, 132846 (2021).

[26] A. Mvogo, J. E. Macias-Diaz, and T. C. Kofané, Diffusive instabilities in a hyperbolic activator-inhibitor system with superdiffusion, Phys. Rev. E **97**, 032129 (2018).

[27] G. Consolo, C. Curró, and G. Valenti, Supercritical and subcritical Turing pattern formation in a hyperbolic vegetation model for flat arid environments, Phys. D (Amsterdam) **398**, 141 (2019).

[28] M. AI-Ghoul and B. C. Eu, Hyperbolic reaction-diffusion equations and irreversible thermodynamics: Cubic reversible reaction model, Phys. D (Amsterdam) **90**, 119 (1996).

[29] M. AI-Ghoul and B. C. Eu, Hyperbolic reaction-diffusion equations and irreversible thermodynamics: II. Two dimensional patterns and dissipation of energy and matter, Phys. D (Amsterdam) **97**, 531 (1996).

[30] G. Consolo, C. Curró, and G. Valenti, Turing vegetation patterns in a generalized hyperbolic Klausmeier model, Math. Methods Appl. Sci. **43**, 10474 (2020).

[31] E. Barbera, C. Curró, and G. Valenti, On discontinuous travelling wave solutions for a class of hyperbolic reaction-diffusion models, Phys. D (Amsterdam) **308**, 116 (2015).

[32] V. Mendez, S. Fedotov, and W. Horsthemke, *Reaction-Transport Systems* (Springer, Berlin, 2010).

[33] V. Mendez, D. Campos, and W. Horsthemke, Growth and dispersal with inertia: Hyperbolic reaction-transport systems, Phys. Rev. E **90**, 042114 (2014).

[34] E. P. Zemskov, M. A. Tsyganov, and W. Horsthemke, Wavy fronts in a hyperbolic FitzHugh-Nagumo system and the effects of cross diffusion, Phys. Rev. E **91**, 062917 (2015).

[35] U. I. Cho and B. C. Eu, Hyperbolic reaction-diffusion equations and chemical oscillations in the Brusselator, Phys. D (Amsterdam) **68**, 351 (1993).

[36] D. G. Milchunas and W. K. Lauenroth, Inertia in plant community structure: state changes after cessation of nutrient-enrichment stress, Ecol. Appl. **5**, 452 (1995).

[37] V. Mendez and J. E. Llebot, Hyperbolic reaction-diffusion equations for a forest fire model, Phys. Rev. E **56**, 6557 (1997).

[38] C. Valentin and J. M. d'Herbés, Niger tiger bush as a natural water harvesting system, Catena **37**, 231 (1999).

[39] K. P. Hadeler, Reaction transport equations in biological modeling, Math. Comput. Model. **31**, 75 (2000).

[40] T. Hillen, Hyperbolic models for chemosensitive movement, Math. Models Methods Appl. Sci. **12**, 1007 (2002).

[41] J. Fort and V. Mendez, Wavefronts in time-delayed reaction-diffusion system, Theory and comparison to experiments, Rep. Prog. Phys. **65**, 895 (2002).

[42] P. Garcia-Fayos and M. Gasque, Consequences of a severe drought on spatial patterns of woody plants in a two-phase mosaic steppe of Stipa tenacissima, J. Arid Environ. **52**, 199 (2002).

[43] B. Straughan, Heat Waves, *Applied Mathematical Sciences* (Springer, New York, 2011).

[44] V. Deblauwe, P. Couteron, O. Lejeune, J. Bogaert, and N. Barbier, Environmental modulation of self-organized periodic vegetation patterns in sudan, Ecography **34**, 990 (2011).

[45] V. Deblauwe, P. Couteron, J. Bogaert, and N. Barbier, Determinants and dynamics of banded vegetation pattern migration in arid climates, Ecol. Monograph **82**, 3 (2012).

[46] R. Hillerislambers, M. Rietkerk, F. van de Bosch, H. H. T. Prins, and H. de Kroon, Vegetation pattern formation in semi-arid grazing systems, Ecology **82**, 50 (2001).

[47] M. Rietkerk, M. C. Boerlijst, F. van Langevelde, R. HilleRisLambers, J. van de Koppel, H. H. T. Prins, and A. de Roos, Self-organisation of vegetation in arid ecosystems, Am. Nat. **160**, 524 (2002).

[48] E. Gilad, J. von Hardenberg, A. Provenzale, M. Shachak, and E. Meron, Ecosystem Engineers: From Pattern Formation to Habitat Creation, Phys. Rev. Lett. **93**, 098105 (2004).

[49] F. Borgogno, P. D'Odorico, F. Laio, and L. Ridolfi, Mathematical models of vegetation pattern formation in ecohydrology, Rev. Geophys. **47**, RG1005 (2009).

[50] E. Meron, From patterns to function in living systems: Dryland ecosystems as a case study, Annu. Rev. Condens. Matter Phys. **9**, 79 (2018).

[51] J. von Hardenberg, E. Meron, M. Shachak, and Y. Zarmi, Diversity of Vegetation Patterns and Desertification, Phys. Rev. Lett. **87**, 198101 (2001).

[52] J. A. Sherratt and A. D. Synodinos, Vegetation patterns and desertification waves in semi-arid environments: Mathematical models based on local facilitation in plants, Discrete Cont. Dyn. Syst. Ser. B **17**, 2815 (2012).

[53] J. A. Sherratt, Pattern solutions of the klausmeier model for banded vegetation in semiarid environments V: The transition from patterns to desert, SIAM J. Appl. Math. **73**, 1347 (2013).

[54] E. Meron, *Nonlinear Physics of Ecosystems* (CRC Press, Boca Raton, FL 2015).

[55] Y. R. Zelnik, H. Uecker, U. Feudel, and E. Meron, Desertification by front propagation? J. Theor. Biol. **418**, 27 (2017).

[56] C. A. Klausmeier, Regular and irregular patterns in semiarid vegetation, Science **284**, 1826 (1999).

[57] K. Siteur, E. Siero, M. B. Eppinga, J. D. M. Rademacher, A. Doelman, and M. Rietkerk, Beyond turing: The response of patterned ecosystems to environmental change, Ecol. Complex. **20**, 81 (2014).

[58] G. Consolo and G. Valenti, Secondary seed dispersal in the Klausmeier model of vegetation for sloped semi-arid environments, Ecol. Model. **402**, 66 (2019).

[59] K. Gowda, S. Iams, and M. Silber, Signatures of human impact on self-organized vegetation in the Horn of Africa, Sci. Rep. **8**, 3622 (2018).

[60] B. Von Holle, H. R. Delcourt, and D. Simberloff, The importance of biological inertia in plant community resistance to invasion, J. Veg. Sci. **14**, 425 (2003).

[61] J. H. Brown, T. G. Whitham, E. S. K. Morgan, and C. A. Gehring, Complex species interactions and the dynamics of ecological systems: Long-term experiments, Science **293**, 643 (2001).

[62] A. Hastings, Transients: The key to long-term ecological understanding, Trends Ecol. Evol. **19**, 39 (2004).

[63] A. Hastings, Transient phenomena in ecology, Science **361**, 6406 (2018).

[64] T. Ruggeri and M. Sugiyama, *Classical and Relativistic Rational Extended Thermodynamics of Gases* (Springer, Cham, 2021).

[65] G. Gambino, S. Lupo, M. Sammartino, D. Lacitignola, I. Sgura, and B. Bozzini, Weakly nonlinear analysis of Turing patterns in a morphochemical model for metal growth, Comput. Math. Appl. **70**, 1948 (2015).

[66] V. Giunta, M. C. Lombardo, and M. Sammartino, Pattern formation and transition to chaos in a chemotaxis model of acute inflammation, SIAM J. Appl. Dyn. Syst. **20**, 1844 (2021).

[67] S. Van der Stelt, A. Doelman, G. Hek, and J. D. M. Rademacher, Rise and fall of periodic patterns for a generalized klausmeier-gray-scott model, J. Nonlinear Sci. **23**, 39 (2013).

[68] W. Van Saarloos, Front propagation into unstable states, Phys. Rep. **386**, 29 (2003).

[69] J. A. Sherratt, Pattern solutions of the Klausmeier Model for banded vegetation in semi-arid environments I, Nonlinearity **23**, 2657 (2010).

[70] Y. R. Zelnik, P. Gandhi, E. Knobloch, and E. Meron, Implications of tristability in pattern-forming ecosystems, Chaos **28**, 033609 (2018).

[71] COMSOL MULTIPHYSICS® v. 5.6. COMSOL AB, Stockholm, Sweden. www.comsol.com.